

Hybrid RANS/LES Simulation of Jet Surface Interaction Noise

Gerrit-Daniel Stich ^{*}, Jeffrey A. Housman, [†]
Joesph G. Kocheemoolayil [‡] and Cetin C. Kiris [§]
NASA Ames Research Center, M/S 258-2, Moffet Field, CA 94035

James E. Bridges [¶] and Clifford A. Brown ^{||}
NASA Glenn Research Center, 21000 Brookpark Road, Cleveland, OH 44212

NASA's Commercial Supersonic Technology (CST) project has formulated a technical challenge to design a quiet propulsion system for a low boom supersonic aircraft that meets Federal Aviation Authority's airport noise regulations with sufficient margin. Several proposed configurations take advantage of shielding from the wing or other air-frame components. Development of carefully validated computational tools are necessary for critically evaluating installation concepts that are currently being proposed to meet the technical challenge. Semi-empirical models that predict the noise reduction potential of arbitrary shielding surfaces are yet to mature. Another key challenge is the systematic assessment of additional noise from the interaction between high speed jet turbulence and a surface in its vicinity. As a first step towards predicting noise reduction due to radical installation concepts from first principles, we simulate the noise generated by a high speed turbulent round jet near a simple planar surface. Detailed comparisons are made with a dedicated experiment conducted at NASA's Glenn Research Center. Sensitivity of far-field noise predictions to grid resolution is systematically documented. A permeable Ffowcs Williams Hawkings (FWH) surface enclosing both the jet and the shielding surface is used to predict far-field noise from the simulated flow-field. Details of the structured overset grids, numerical discretization, and turbulence model are provided. Near-field comparisons to PIV data and far-field comparisons to microphone array measurements are discussed. Excellent agreement for an initial validation study on an isolated free round jet was obtained and the findings were utilized in the jet surface interaction study. The split between shielded and reflected side of the microphone array was captured with good agreement, as well as the peak in the noise spectra due to scattering of turbulent energy into sound by the trailing edge of the surface.

I. Introduction

NASA's Commercial Supersonic Technology (CST) project has formulated a technical challenge to design a quiet propulsion system for a low boom supersonic aircraft that meets Federal Aviation Authority's airport noise regulations with sufficient margin. In recent years, two distinct approaches are being investigated to reduce jet noise. One approach is optimizing the nozzle geometries to increase entrainment. The other approach is to take advantage of shielding from the airframe by using novel integrated propulsion concepts. An approach that combines complementary ways of reducing jet noise targeting both enhanced entrainment through devices such as chevrons and shielding through radical installation concepts will most likely be necessary to address the significant challenges posed by airport noise regulations for commercial supersonic aircraft. Within this context, the development of carefully validated computational tools for critically evaluating proposed concepts for low noise propulsion is a key pacing item. Semi-empirical models that predict the noise reduction potential of arbitrary shielding surfaces are yet to mature. Another key challenge is the systematic assessment of additional noise from the interaction between high speed jet turbulence and a surface in its vicinity[1, 2]. It is now widely accepted that trailing edge noise is expected to make a sizable contribution to the overall noise signature for several modern aircraft configurations that place the engine exhaust in close proximity to the

^{*}Science and Technology Corporation, AIAA Member, gerrit-daniel.stich@nasa.gov

[†]Computational Aerosciences Branch, AIAA Senior Member, jeffrey.a.housman@nasa.gov

[‡]Science and Technology Corporation, AIAA Member, joseph.g.kocheemoolayil@nasa.gov

[§]Computational Aerosciences Branch, AIAA Senior Member, cetin.c.kiris@nasa.gov

[¶]Acoustics Branch, AIAA Associate Fellow, james.e.bridges@nasa.gov

^{||}Acoustics Branch, AIAA Associate Fellow, clifford.a.brown@nasa.gov

airframe [3, 4]. Several future designs integrate propulsive and aerodynamic components of the aircraft even closer in search of greater aerodynamic performance. Hence the issue of additional noise sources is only likely to become an even more pressing concern in the future.

Jet noise predictions utilizing computational fluid dynamics (CFD) solvers have been reported for more than four decades [5–8]. A review of the methods and accuracy of the simulations prior to 2008 is described in Bodony and Lele [9]. While great advancements have been made towards predicting jet noise with CFD solvers including high-fidelity simulations at flight Reynolds numbers, as well as some inclusions of simple but important geometric features such as jet surface interaction noise, most simulations reported in the literature rely on high fidelity wall-modeled Large-Eddy simulation (WMLES) and are still limited to simple geometries due to the complexity of the problem. Due to the need for computationally demanding scale-resolving simulations in order to predict accurate far-field noise it is still computationally too demanding to investigate full air frame interaction noise using the previously mentioned methods. A possible strategy to advance towards full-scale airframe simulations including jet-noise prediction is the use of a hybrid RANS/LES approach. In this approach most parts of the aircraft are simulated utilizing computationally less demanding unsteady RANS, while critical areas in which most of the noise is created are simulated using LES. In order to predict jet noise on a full flight configuration airplane, the modeling and simulation practices and the use of hybrid RANS/LES methods must be scrutinized and new methods need to be developed.

The emphasis of this work is on demonstrating jet noise prediction capabilities within the Launch Ascent and Vehicle Aerodynamics (LAVA) framework, which can already handle complex geometries, flight Mach and Reynolds numbers, and has been used for several airframe aeroacoustic problems [10–13]. Previous simulations focusing on free-jet noise on a similar geometry have been carried out with good agreement [14]. Additional free jet simulations are carried out in this work as an initial validation study in Section IV.B. As a first step towards predicting noise reduction due to radical installation concepts from first principles, we simulate the noise generated by a high speed turbulent round jet near a simple planar surface. Detailed comparisons are made with a dedicated experiment conducted at NASA’s Glenn Research Center and presented in section IV.C. Sensitivity of far-field noise predictions to grid resolution is systematically documented. A permeable Ffowcs Williams Hawkings (FWH) surface enclosing both the jet and the shielding surface is used to predict far-field noise from the simulated flow-field. Section V summarized the work and gives a perspective on future and current approaches to predict noise reduction associated with radical installation concepts.

II. Problem Description

The corresponding jet surface interaction tests were conducted at the Small Hot Jet Acoustic Rig (SHJAR), which is located in the Aeroacoustic Propulsion Laboratory (AAPL) at NASA Glenn Research Center [15, 16]. Figure 2 (a) shows a perspective picture of the SHJAR including the test nozzle and microphone layout with 24 microphones on the left side of the image. Note that the nozzle axis in the downstream flow direction is marked as 180° in the experimental coordinate system. The SHJAR was commissioned in 2001 to test jet noise reduction concepts and develop advanced measurement techniques and is capable of supplying air at flow rates up to 2.7 kg/s to a single-nozzle stream. Details of the SHJAR, the measurement techniques used to acquire the near-field and far-field data, and validation of experimental results are presented in Refs. [1, 17]. The baseline axisymmetric convergent Small Metal Chevron (SMC000) nozzle, shown in Figure 2b is used for the current study. It has been stripped of all drill holes and additional attachment hardware to simplify the meshing. The bottom part of the picture shows a cut through the center line in order to visualize the nozzle interior. The SMC000 nozzle has an exit diameter of 2", and in the jet-surface experiments a 12 inch extension was added between the initial contraction and the final contraction. As propulsion noise is the primary source of sound during take-off, flight conditions between $0.5 \leq Ma \leq 0.9$ where considered in the experiments. The test conditions used for this study are referred to as Set Point 7 (SP7) with an acoustic Mach number of $U_{jet}/c_\infty = 0.9$, a jet temperature ratio of $T_{jet}/T_\infty = 0.835$, nozzle pressure ratio of $P/P_\infty = 1.861$, a jet Mach number of $U_{jet}/c_{jet} = 0.985$, and Reynolds number of 1 million based on the nozzle diameter D_j . These conditions are consistent with those reported in a previous study by the authors [14]. A flat plate in close proximity to the axisymmetric nozzle was used in order to assess surface interaction noise and jet-shielding capabilities. The configuration can be seen in Figure 3. The distance from the plate to the nozzle center-line h/D_j was articulated by an automated traverse between $0.5 \leq h/D_j \leq 5$ in the experiments. A bulge has been added at the leading edge of the plate in order to accommodate the nozzle for the $h/D_j = 0.5$ configuration. The cutout of this bulge can be seen in Figure 2 For this study only a distance of $h/D_j = 1$ is considered. The plate has a thickness of 0.5 inch and is beveled with a 45 degree angle at the trailing edge. Due to

the close proximity of the plate to the jet, additional flow features such as a secondary shear layer at the trailing edge, trailing edge noise as well as a secondary boundary layer are introduced that complicate this problem compared to a single round jet. Near-field PIV data and far-field microphone data acquired in the SHJAR for Set Point 7 using the SMC000 nozzle were provided by NASA Glenn Research Center for validation [1, 17].

III. Computational Methodology

The LAVA solver framework [18] is utilized for the computational study. LAVA offers flexible meshing options and was developed with the intent of modeling highly complex geometry and flow-fields. The framework supports Cartesian and curvilinear structured grids as well as unstructured arbitrary polyhedral meshes. Overset grid technology [19] is used to couple the solutions across different overlapping meshes. In this study, the structured curvilinear overlapping grid methodology is used with a hybrid RANS/LES method (ZDES Mode III). The curvilinear overset grids are generated utilizing the PointwiseTM and Chimera Grid Tools (CGT) [20] software packages.

A. Curvilinear Navier-Stokes Solver

The compressible hybrid Reynolds Averaged Navier-Stokes/Large Eddy Simulation (RANS/LES) equations are solved using a finite-difference formulation applied to the curvilinear transformed system of equations in strong conservation law form. The Spalart-Allmaras (SA) [21] turbulence model is used as the base RANS closure model. A zonal hybrid RANS/LES method as well as unsteady RANS is used in this paper. Implicit second-order backward differencing (BDF2) is used for time integration and the discretized equations are marched in pseudo-time until a sufficient reduction in the residual has been achieved for each physical time-step (approximately 3 to 4 orders of magnitude of residual reduction is achieved in the present computations). The nonlinear system of equations are linearized at each pseudo time-step and an alternating line-Jacobi relaxation procedure is applied. A local pseudo time-step corresponding to a Courant-Friedrichs-Lowy (CFL) number of 10 is used to accelerate convergence. Domain decomposition and the Message Passing Interface (MPI) are used to enable a scalable parallel algorithm.

1. Low Dissipation Finite-Difference Method

High-order accurate low dissipation finite-difference schemes have been shown to be an effective strategy for turbulence resolving simulations using LAVA [11, 12, 22–24]. A thorough study comparing several high-order finite-difference methods on Cartesian grids within the LAVA framework was reported previously [25]. Results from this study indicated that high-order Weighted Essentially Non-Oscillatory (WENO) schemes [26] performed well in both resolution (Points-Per-Wavelength PPW), shock capturing, and robustness under harsh flow conditions. A natural extension of finite-difference WENO schemes to curvilinear grids are the high-order Weighted Compact Nonlinear Schemes (WCNS) [27]. The WCNS method, applied to the convective fluxes, consists of WENO interpolation (as opposed to reconstruction) of the left and right states to the half grid points, followed by evaluation of the numerical flux at the half points by an approximate (or exact) Riemann solver or flux vector splitting scheme, and concluding with a high-order central finite-difference operator at the grid points which depends on the numerical fluxes at the half points in either an implicit (i.e. compact) or explicit form. When applying finite-difference methods to the curvilinear equations in strong conservation law form, standard WENO finite-difference methods will not satisfy the Geometric Conservation Law (GCL) making it necessary to combine the WENO interpolation with high-order central-difference operators. It has been shown that free-stream preservation (i.e. the GCL condition) is satisfied up to machine precision provided that consistent central difference operators are used for discretizing the metric terms as well as the fluxes [28, 29]. An additional advantage of WCNS over WENO is the ability to use approximate Riemann solvers. Standard finite-difference WENO methods require the use of flux vector splitting methods for numerical flux evaluation. In this work, a modified version of the Roe numerical flux is used [30–32].

A consequence of using high-order central difference operators applied to numerical fluxes at the half grid points, which depend on high-order WENO interpolation, is the much wider stencil required for the same order of accuracy compared to the standard finite-difference WENO method. To reduce this pathology, high-order central difference operators using a combination of the numerical fluxes at the half grid points and the physical fluxes at the grid points have been developed [33, 34]. This approach, denoted Hybrid Weighted Compact Nonlinear Scheme (HWCNS), allows for up to third/fourth-order accuracy using a five-point stencil by combining blended third- and fourth-order

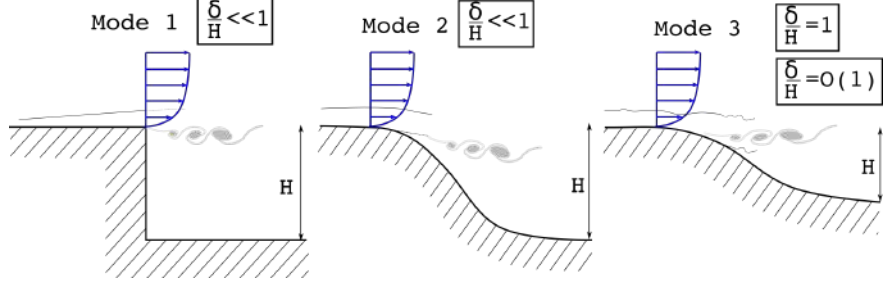


Fig. 1 Classification of canonical flow problems by mode following Deck *et al.* [44]: (1) separation fixed by geometry, (2) separation induced by pressure gradient on curved surface, (3) separation strongly dependent on dynamics of incoming boundary layer.

interpolation with a fourth-order hybrid central difference operator. In the current approach, the convective fluxes (and the metric-terms used within) are discretized with the high-order HWCNS, while the viscous fluxes (and their metric terms) are discretized with standard second-order accurate central differencing. A more detailed description is included in Housman *et al.* [23].

2. Hybrid RANS/LES model

The Detached Eddy Simulation [35, 36] (DES) and Delayed Detached Eddy Simulation [37–39] (DDES) turbulence model closures are well-tested hybrid RANS/LES models for highly separated flows. In the original DES model, the transition between RANS and LES models was based strictly on local mesh size relative to the wall-distance. For geometries with a wide range of geometric length scales, such as high-lift devices with finite-thickness leading and trailing edges or nozzles with finite thickness exits, the local mesh spacing may become small enough to force transition from the RANS model to the LES model, but the mesh is typically not small enough to resolve the unsteady fluctuations causing the well-known modeled stress depletion [40]. This resulted in a modification denoted as DDES, which attempts to remain in RANS mode in the attached boundary layer [37]. Inspection of the shielding function often shows a strange behavior of going from RANS near the wall, to LES, back to RANS just past the edge of the boundary layer, and subsequently back to LES [41]. This behaviour has previously been observed for a similar jet configuration which resulted in a significant delay in the development of three-dimensional structures [13, 14].

An alternative strategy appropriate for structured multi-block and overset grids is the Zonal DES (ZDES) approach first introduced by Deck [42–44] in which specific zones are designated to use the RANS, DDES, or LES models explicitly. This idea of zonal specification has been further generalized to include a user-specified wall distance based transition location between RANS and LES [45, 46]. This allows the user to choose, based on a strong understanding of the physics of the problem, which regions should be solved in pure RANS and hybrid RANS/LES mode. When in hybrid RANS/LES mode it also gives additional control to the user to prescribe the transition location to explicitly guarantee that the attached boundary layer remains in RANS mode. This is very important since shielding functions, such as those used in the DDES model, can still fail when the mesh is fine enough to capture some three-dimensional fluctuations, but not fine enough to resolve the relevant scales in the boundary layer to accurately predict skin friction.

A recent extension to ZDES, introduced by Deck *et al.* [44, 47, 48] and improved by Renard *et al.* [49], in which the model acts in a wall-modeled LES (WMLES) mode has also been added to LAVA. Here RANS is used in the inner layer of the attached boundary layer up to a user selected wall distance (typically 10% of local BL thickness [49]), and interfaces to an outer LES (no forcing or filtering is applied). This is a simple and robust approach which avoids spurious artifacts at the interface, however it can lead to a log-layer mismatch caused by the inconsistency in the equation set across the interface (i.e. Reynolds averaged Navier-Stokes on one side of the interface and filtered Navier-Stokes on the other side).

The ZDES approach used in this paper is based on the Spalart-Allmaras (SA) [21] turbulence model, where the pseudo viscosity $\tilde{\nu}$, from the model scales with the distance to the wall d_w and the local vorticity magnitude Ω in the inner layer. In the outer LES region the SA model acts as a subgrid-scale model (SGS) with a modified length scale for d_w . For this reason Deck introduced three different hybrid length scale formulations replacing d_w with d_{ZDES} which were optimized for canonical flow configurations (see Figure 1). Only Mode III, which is calibrated for flows where

the separation is strongly influenced by the dynamics of the incoming boundary layer, will be considered in this study. The user must select which zones to solve in pure RANS mode and which zones to apply ZDES Modes I, II, or III. For zones which use ZDES Mode III, the user must also prescribe an interface distance from the wall h_w at which to transition from RANS to LES. A detailed discussion about the interface location can be found in Stich *et.al.* [13]. The user must also supply turbulent fluctuations at the inflow (Sec. III.B). The hybrid length scale for Mode III is defined in the following way:

$$d_{ZDES} = \begin{cases} d_w, & \text{if } d_w < h_w \\ \min(d_w, C_{DES} \cdot \Delta), & \text{otherwise} \end{cases} \quad (1)$$

with the constant $C_{DES} = 0.65$ and the subgrid length scale $\Delta = (\Delta x \Delta y \Delta z)^{1/3}$. In this work we focus on ZDES Mode III only. An interface location of $h_w = 0.1\delta_0$ is chosen for this work.

B. Turbulent Inflow Generation - Synthetic Eddy Method

The noise produced by attached boundary layers, such as the boundary layer near a nozzle exit, are highly dependent on the three-dimensional turbulent structures near the wall. These turbulent structures also significantly influence the development of the turbulent jet shear layers emanating from the nozzle exit which dictate the accuracy of the far-field acoustic prediction [50]. Non-zonal methods, such as DDES, are known to be less accurate for these types of flows, and only Direct Numerical Simulation (DNS) and wall-resolved LES are truly capable of modeling these turbulent structures deep in the boundary layer [51]. Since wall-resolved LES of even small portions of the nozzle interior, near the nozzle exit, are still not affordable for realistic Reynolds numbers, an alternative strategy must be developed. One approach is to utilize wall-modeled LES [50, 52, 53] which substantially reduces the meshing requirements compared to wall-resolved LES. In the current approach, the ZDES Mode III model described above is used in the nozzle interior, just upstream of the nozzle exit. The d_0 parameter is chosen such that the model transitions from RANS to LES at approximately $y^+ = 100$ based on the nozzle exit boundary layer predicted using a preliminary RANS analysis. Since no turbulent fluctuations are resolved in the pure RANS zones in upstream nozzle interior, artificial turbulent fluctuations (LES inflow) must be added at the interface between the RANS and LES zones to facilitate the development of resolved turbulent structures in the outer-region of the boundary layer where the LES model is activated.

The synthetic eddy method (SEM) of Jarrin *et.al* [54, 55] is used to generate turbulent structures in the upstream boundary layer. This approach introduces synthetic eddies at the interface, such that first and second order turbulent statistics are matched with the upstream RANS solution. The eddies are convected at a characteristic velocity (based on the averaged streamwise velocity at the seeding plane) in order to mimic the temporal and spatial correlations of actual three-dimensional turbulence. Although the interface will converge to the correct first and second order statistics, there is a delay before physical 3D turbulence is recovered within the flow field. This can be observed in the RMS of the stream-wise velocity. Some modifications of the formulation have been made regarding the size of the eddies [56]. For the jet-noise simulations the SEM interface is placed approximately 53 nozzle exit boundary layer thicknesses upstream of the nozzle. In a previous channel flow simulation around 30 BL thicknesses were required to recover skin friction, some additional margin was added to account for the convergent part at the nozzle exit. The correlation length scales used in this implementation are computed (see Eqn. 2) using Bradshaw's hypothesis [57] to compute the turbulent kinetic energy.

$$\sigma_{SEM} = \max \left(\min \left(2d_w, 3 \frac{k^{2.5}}{\epsilon} \right), 1.5\Delta \right), \quad (2)$$

where $\Delta = \max(\Delta_x, \Delta_y, \Delta_z)$, d_w the wall distance and $\epsilon = 0.09k^2/\nu_t$ the rate of dissipation. The turbulent kinetic energy k is computed with $k = \frac{\nu_t |S|}{c_\mu}$.

IV. Computational results

High-fidelity time-accurate simulations were performed to assess the capability of the LAVA ZDES Mode III model with the low dissipation finite-difference method to predict jet noise accurately. First the results of an initial validation study on the isolated round jet geometry are presented. Second results from the case with an inserted plate at 1D away from the nozzle centerline are presented. A time-step of 0.005 in convective units ($\Delta t * c_\infty / D_j$) is used for all of

simulations along with 5 – 10 sub-iterations which equated to 3 – 4 orders of magnitude residual reduction at each physical time-step of the dual-time stepping algorithm. This time-step in viscous wall units computed at the nozzle exit is $\Delta t^+ \approx 10$. If an explicit time-marching scheme is used with the current mesh and a CFL restriction of unity is enforced, then the time-step would need to be reduced three orders of magnitude compared to the current simulation because of the viscous wall spacing. To begin the simulations, unsteady RANS is performed at a larger time-step 0.5 in convective units for a sufficiently long duration until a nearly steady solution is obtained. Next, the ZDES Mode III model was activated and 20,000 time-steps were performed to flush-out the transients created by activating the hybrid model (this includes activation of the SEM). Finally an additional 30,000 time-steps for the isolated jet and 120,000 time-steps for the surface interaction configuration were performed and turbulent statistics were computed over these time histories. This is equivalent to a simulation for the isolated case of 330 convective time units ($T_{sim}c_\infty/D_j$) with statistics computed over 200 convective time units. For the case with shielding plate, statistics were computed over 800 convective time units, to account for the fact that circumferential averaging of the flow statistics and noise spectra is not possible due to the asymmetry.

The computational resources utilized where 1940 cores for the coarse (90M), 1940 cores for the medium (120M) and 2400 cores for the fine (210M) simulation. The initial unsteady RANS simulations were run for 12 hours, then the remaining ZDES Mode III simulations required 5 – 15 days for the 20,000-120,000 time-steps depending on the number of points per core and the number of time-steps. All simulations were performed on the Pleiades cluster at NASA Ames Research Center using Intel Xeon E5-2680v4 processors.

A. Structured Overset Grid System

The advantage of structured overset grids for aeroacoustic analysis of jet noise includes the ability to generate highly anisotropic grids to capture nozzle boundary layers and shear layers and to locally refine the meshes in the azimuthal direction at different streamwise and radial locations along the jet axis. Structured grid flow solvers are typically highly efficient, have a low memory footprint, and offer a straightforward and inexpensive extension to high-order low dissipation finite-difference discretization. Allowing the structured grids to overlap each other not only simplifies the process of generating the grids (in comparison to structured multi-block abutting grids), it also allows for high quality (less-skewed) meshes.

Three different mesh resolutions have been derived for the isolated free round jet configuration of the SMC000 nozzle following the specifications detailed in Bogey *et. al.* [58] which used structured multi-block grids. Tight-clustering is used near the viscous walls to guarantee a $\Delta y^+ \approx 1$ throughout the nozzle interior. Different streamwise mesh spacing have been applied adapting the guidelines by Bres *et.al* [5, 6] for unstructured grids. The finest streamwise mesh spacing used at the nozzle lip is extended along the downstream jet axis to provide adequate resolution across the shear layer of the jet in the axial direction up to $0.1D_j$ as well as in radial direction inside the shear layer. The streamwise as well as circumferential mesh spacing can be seen in Table 1. A stretching ratio of 1.014 in streamwise direction is applied until the maximum spacing in each region is reached and kept constant from there (e.g. start with $\Delta x = D_j/71$ at $x/D_j = 1$ stretch it with 1.014 until $\Delta x = D_j/60$ is reached from there it is kept constant until the next region at $x/D_j = 10$). After $30D_j$, the mesh is stretched geometrically with a stretching ratio of 1.05 to a far-field distance of 280 nozzle diameters. Figure 4 (a) depicts a cutting plane through the jet centerline on the fine mesh showing the tight mesh clustering in radial direction extending outwards of the nozzle lip in order to adequately capture the jet shear layer. A uniform spacing in radial direction is pursued at around $6D_j$ and downstream where the potential core breaks down. As no multiblock capability was available within the LAVA curvilinear overset solver at the time this work was performed, an overset lip mesh had to be utilized in order to avoid orphan points created by budding grids at the nozzle lip (see Detail A in Figure 4). Special care has been taken to keep this lip mesh within the RANS part of our ZDES Mode III simulation, as generation of spurious noise from overlapping meshes within the boundary layer has been observed in previous simulations. Benefits of varying the circumferential spacing at different axial and radial locations were reported in Bres *et.al.* [50] and Housman *et.al* [14]. The number of points in the circumferential direction at four different radial sections are given in Table 1. The finest circumferential spacing is used close to the nozzle geometry as well as in the shear-layer downstream of the nozzle lip. The variation of circumferential spacing in radial direction can be seen in the streamwise cuts in Figure 5 for the fine mesh (b) and coarse mesh (a). In this work, a maximum coarsening factor of 2:1 is utilized at each mesh interface in which the overset information between each grid is communicated. It should be recognized that although these grids are relatively large compared to some previous studies [59, 60], they are significantly coarser than the suggested spacings for wall-modeled LES [61, 62]. For example, the number of azimuthal grid points suggested in Ref. [62] for wall-modeled LES based on $\Delta s_{azimuth} = 0.05\delta_{exit}^{BL}$ is 4911 points, where δ_{exit}^{BL} is

the boundary layer height at the nozzle exit computed from the RANS calculation. While the number of azimuthal grid points suggested for wall-resolved LES based on $\Delta s_{azimuth}^+ = 10$ is 25,852 points. Note that these estimates may be excessive and high quality results may be achievable using LES with much coarser spacings [5, 50]. Using the above described method resulted in 90M grid points for the coarse mesh, 120M grid points for the medium and 210M grid points for the fine mesh. In order to avoid the singularity at the jet centerline, a core mesh was included utilizing the overset approach.

For the jet-shielding case, a separate mesh containing the plate has been created and combined with the medium mesh resolution of the isolated case taking advantage of the overset capability. For this purpose, a mesh with near to isotropic cells (except in the boundary layer) has been created adding an additional 130M grid points. As waves reflected and shielded by the plate even at the far edge of the plate have to be adequately resolved, this large number of points in comparison to the isolated case has been necessary due to the large streamwise and spanwise extent of the plate geometry of $8D_j$ and $12D_j$ respectively. The mesh containing the plate grid can be seen in Figure 4 (a) and (b).

Table 1 Streamwise mesh spacing at given axial locations downstream of nozzle exit and number of points in circumferential direction at given radial locations. Refinement ratio in overset regions never exceeds 2:1.

mesh resolution	streamwise points per D_j				circumferential points			
	$x = 0.1D_j$	$x = 1D_j$	$x = 10D_j$	$x = 25WD_j$	Θ_1	Θ_2	Θ_3	Θ_4
coarse	250	45	45	40	354	178	90	90
medium	300	61	54	45	708	354	180	90
fine	300	71	60	54	1416	708	354	180

B. Isolated Round Jet Validation

In order to predict the noise generated by a plate in close proximity to a round jet, it is necessary to gain a better understanding of the isolated free round jet first. For this purpose the isolated round jet geometry has been investigated on three different mesh resolutions. A jet with similar conditions (SP7) and geometry has been previously investigated by the authors [14]. The configuration studied in this work poses a modification to the initially investigated geometry by adding a 12" straight section before the final convergent portion of the nozzle. This results in a significantly different boundary layer profile within the nozzle, which has an effect on the noise as well as the near field results. This will be addressed in more detail in the following sections.

1. Flow Field Visualizations and qualitative description

An instantaneous snapshot of the vorticity magnitude for the isolated unheated ideally-expanded round jet is shown in Figure 5 (a) and (b) and illustrates the detailed turbulent structures which are well resolved in the fine simulation. The mesh is also shown partially at streamwise planes showing the refinement in circumferential direction in the fine simulation, where it was kept constant in the coarse simulation (see Table 1). At approximately $6D_j$ where the potential core breaks down, constant mesh spacing in radial direction was used (see cutting plane at $x/D_j = 10$). The thin laminar shear layer transitions quickly to turbulence within $1D_j$ downstream of the nozzle for the fine simulation. No significant grid effects due to the reduction of points in circumferential direction on the mixing of the turbulent flow further downstream can be observed.

The coarse simulation shows quasi two-dimensional vortical structures near the nozzle exit. This can also be observed by looking at the instantaneous iso-contour of the Q-criteria depicted in Figure 6 colored by the normalized axial velocity magnitude. These structures which are caused by insufficient resolution in circumferential direction are not physical and trigger spurious acoustic waves which propagate to the far-field. The increase of the mesh resolution in circumferential direction allows the resolution of smaller eddies in the shear layer which further reduces the quasi two-dimensionality. For the medium mesh these coherent structures break down further and look more "waffle-cone" like structures which reduce even further for the fine simulation. By including a synthetic eddy method in order to seed turbulent structures within the nozzle interior roughly $30D_j$ upstream of the nozzle exit, these waffle cone structures vanish completely. Figure 7 illustrates a more global view of the flow field. The general structure of the flow is visualized by the iso-contour of the Q-criteria colored by the axial normalized velocity in (a) where the sound created by the flow

is visualized on cutting planes showing the magnitude of the pressure gradient on two cutting planes and the density gradient magnitude in sub-figure (b) both in grey-scale. The merging of the three-dimensional turbulent structures in the jet shear layer at the end of the potential core and the acoustic waves generated by the potential core breakdown and shear layer mixing are clearly illustrated. The occurrence of high frequency acoustic waves near the jet shear-layer can also be clearly seen. Sound waves created due to Mach wave radiation [63, 64] in the 150.0° observer direction (where 180.0° aligns with the downstream jet axis), as well as noise emitted due to the breakdown of turbulent eddies downstream of the flow can also be seen.

2. Comparison to Experimental Data: Near-Field

Near-field turbulent statistics were computed for the isolated baseline case along the jet axis and at different cross-flow planes and are compared with PIV data from the SHJAR [65] published in Brown and Wernet [17]. The difference between the simulations in this study and simulations previously reported in Housman *et.al.* [14] is the extension of the nozzle geometry with a 12" straight section before the final convergent nozzle section. This extension leads to a significant difference in the development and thickness of the boundary layer inside of the nozzle. The difference in boundary layer thickness gets smaller at the convergent section of the nozzle (see Figure 8).

The quality of a CFD simulation is often measured by the accuracy in the prediction of the potential core length as well as the prediction of the peak turbulent kinetic energy on the jet centerline. Hence within NASA's Revolutionary Computational Aerosciences (RCA) challenge [66], which is part of NASA's CFD vision 2030 project, an improvement in the prediction of those metrics by a factor of 40% compared to state-of-the-art RANS simulations is targeted. The length of the potential core is taken as the distance up to which the centerline velocity is larger than 98% of the jet exit velocity. The reported length of the potential core from the experiment is $X_C = 5.9D_j$ for the nozzle with a 12" extension and as $X_C = 6.95$ for the nozzle without the 12" extension. Figure 9 compares the centerline (a) time-averaged axial velocity, (b) turbulent kinetic energy (TKE) normalized with the nozzle exit diameter D_j for the simulation on all three mesh refinement levels. The experimental results from the shorter SMC000 nozzle are also plotted for comparison. The medium and fine simulations appear to capture the length of the potential core as well as the decay rate of the axial velocity with good agreement. Capturing the length of the potential core is challenging and CFD solvers generally under-predict those quantities when using scale-resolving simulations [5, 67–69] and grossly over-predict the length of the potential core when using conventional RANS turbulence models like the Spalart-Allmaras one-equation turbulence model. The under-prediction is typically due to the insufficient resolution in the jet plume and the delayed transition towards turbulent structures in the nozzle shear layer. With a length of the potential core of $X_C = 5.75$ and $X_C = 5.8$ for the medium and fine simulations the prediction is within 2.5% of the measured value, whereas the coarse simulation under-predicts with $X_C = 4.9$. In comparison, the RANS simulations conducted for this case lead to an over-prediction of around 30% in the length of the potential core. This demonstrates the fact that scale resolving simulations like the ZDES Mode III method used in this paper can fulfill the RCA challenge and show an improvement of more than 40% in the prediction of the potential core. Excellent agreement can also be observed with centerline TKE values, the slightly premature rise in TKE levels can be explained by the shorter length of the potential core. The peak turbulent kinetic energy is captured both in magnitude and location. Figure 10 depicts the axial normalized velocity at five different axial locations relative to the length of the potential core $X_C = 5.9$. Good agreement is achieved with both the medium and fine resolution. The slight under-prediction of the peak velocity at at $x/X_C = 1.075$ is due to the shorter length of the potential core and the slight over-prediction of the peak at $x/X_C > 2.6$ results from the shallower decay of the centerline velocity in our simulation. The fine mesh simulation appears to improve this comparison.

3. Comparison to Experimental Data: Far-Field

The purpose of this section is to gain a better understanding of the propagated far-field noise using the permeable Ffowcs Williams-Hawkins (FWH) method within LAVA [18] and to build best-practice guidelines which can be used for more complex cases like the plate-shielding demonstrated in the next section. In particular it has been observed that the choice of an appropriate FWH surface can significantly influence the result of a simulation, however there is no clear consensus in the literature on how to exactly place the surface triangulation. Parametric studies to assess the sensitivity of far-field noise prediction to the FWH surface choosen can be found in Rahier *et.al.* [70], Uzun *et.al.* [51], Shur *et.al.* [59, 60], Bres *et.al.* [5, 6]. Choosing an appropriate FWH surface generally depends on the mesh resolution and the numerical scheme used. A trade-off has to be made between how close to the jet the FWH surface needs to be in order to accurately capture the waves propagating within the CFD grid while still containing all relevant noise

sources. Another limiting factor on how close the surface can be to the jet is that hydrodynamic fluctuations crossing the permeable FWH surface can result in spurious contributions to the far-field noise spectra. The spurious contribution is caused by ignoring the volume integral of the quadrupole term in the FWH formulation. This can partially be addressed by using phase-averaging over the surface, which is generally done at the end-caps of the triangulation [69].

In order to carefully document the sensitivity to the chosen FWH surface, time-accurate volume data from the isolated round jet simulations was written to disk at a frequency of $F_{max} = 50,000$ Hz. The volume solutions have been interpolated to the triangle centers using the same tri-linear interpolation routines used for the fringe points in the overset solution algorithm. This allows to independently perform parametric studies and serves as a database for further post-processing.

The particular formulation of the frequency-domain permeable surface FWH equations used in LAVA is similar to that presented in Lockhard [71]. The formulation is equivalent to the one used by Bres *et. al.* [5, 50]. The one exception is the substitution of the density perturbation with pressure perturbation, $\rho' := \rho_\infty + p'/c_\infty^2$, suggested by Spalart *et. al.* [72]. Construction of the FWH surface followed some of the best practices outlined in Bres *et. al.* [5] and Mendez *et. al.* [73] for the axisymmetric round jet configuration. The placement of these different surface triangulation's is shown in Figure 11. A detailed comparison of the use of end-cap averaging between $25D_j$ and $30D_j$ to remove spurious contributions from hydrodynamic pressure fluctuations crossing the FWH surface compared to an open FWH surface where both the upstream and downstream ends are extended to cover the entire domain was conducted. Findings similar to Bres *et.al.* [5] were made showing an impact on the Power Spectral Density (PSD) values for Strouhal numbers smaller than 0.5 and therefore are not presented in this paper.

The far-field propagation utilizes the last 30,000 time-steps ($30,000 \Delta t c_\infty / D_j = 200$ convective time-units) of the simulation. This is equivalent to a frequency resolution of $\Delta f = 42$ Hz with a maximum frequency of $F_{max} = 50,000$ Hz. This corresponds to a Strouhal number range of $St_{min} = \Delta St \approx 0.007$ to $St_{max} \approx 8$. Following the procedure outlined in Refs. [5] and [50], the total time sample is sub-divided into 5 windows (or segments) with 50 percent overlap, each window has a Strouhal resolution of $\Delta St_{window} = 0.02$. For each time-window a Hanning filter is applied to the time-domain FWH integrands after the mean has been subtracted, then the Fast Fourier Transform (FFT) is applied to transform the integrands into the frequency domain. Windowing has the effect of reducing spurious noise at the low frequencies caused by spectral leakage. This is very important for the quieter sideline angles ($\Phi < 120^\circ$). Once the FFT is complete, the FWH surface intergrals are evaluated, in the frequency domain, for each observer location to construct the acoustic pressure p' . During the calculation of the PSD, a filter correction factor of $\sqrt{8/3}$ is applied to correct for the energy lost from the windowing procedure. The PSD is then averaged independently over 360 observers for each of the 5 windows. Finally, the 5 windows are averaged and the resulting spectrum is compared to the experimental results (computed over a much larger time-window, i.e. $\Delta St_{exp} = 0.002$). The positioning of the observer angle in the microphone array can be seen in Figure 12. Note that the 180° direction falls on the downstream jet axis.

Figure 13 shows the comparison of the far-field power spectral density (PSD) $100D_j$ away from the nozzle exit for the observers at $\Phi = 60^\circ$, $\Phi = 90^\circ$, $\Phi = 120^\circ$ and $\Phi = 150^\circ$ taken from the fine mesh without SEM. The permeable FWH surface triangulations follow the external nozzle shape with a consistent offset and then radially flare out at $x/D_j = 0$ with $y/D_j = 0.55$ or $y/D_j = 0.6$ at a slope of 0.10, 0.11 or 0.12. The slopes follow typical estimates of the jet spreading ratio [74]. Generally a good agreement is observed in the narrow-band spectrum for all observer angles considered in this study. The peak Strouhal frequency is well-captured. A stronger-decay for the surfaces which are wrapped looser (start of flare at $y/D_j = 0.6$ with slope larger then 0.10 and start of flare at $y/D_j = 0.55$ with slope larger than 0.11) around the jet for high frequencies can be observed. This is due to the numerical dissipation in the scheme used (which needs at least 9 points per wavelength in order to accurately propagate acoustic waves) and the less isotropic cells further away from the jet due to stretching. Opposite behaviour can be observed for a surface that is wrapped too tight around the jet (start of flare at $y/D_j = 0.55$ with slope of 0.10) where hydrodynamic fluctuations cross the surface triangulation at multiple locations causing an increase in the predicted PSD data. A similar behavior however with less deviation has been shown by Bres *et.al* [5]. The smaller sensitivity to the variation of their surface triangulation is due to their less dissipative scheme which allows propagation of acoustic waves in coarser mesh regions and their more isotropic grids. In order to reduce this sensitivity to the choice of the surface triangulation a less dissipative kinetic energy conserving scheme is currently under investigation within the LAVA solver framework [75]. A possible solution in order to make the choice of an appropriate FWH surface triangulation more predictive and in order to have an error estimate to asses the quality of the interpolation one can assess the cell quality of the underlying CFD mesh in regards to wavelength resolution of interest.

Figure 14 shows the influence of inflow turbulence on the far-field acoustics shown on the fine mesh. The synthetic eddy method by Jarrin *et.al.* [54, 55] was used in order to seed inflow turbulence inside of the nozzle at $35D_j$ upstream

of the nozzle exit. This is a common practice for state-of-the-art acoustic jet noise simulations in order to force a more rapid transition towards three-dimensional structures at the nozzle exit in the shear-layer [50]. However, this method introduces spurious contributions to the far-field noise which may not be negligible at high frequencies where the noise level is low. Yet in a previous study using the SP7 SMC000 nozzle without extension [23], no such behaviour could be observed. This is in contrast to our latest findings on the extended nozzle geometry. Especially for the in-plane angle $\Phi = 60.0^\circ$ and $\Phi = 120.0^\circ$ a significant influence of the synthetic eddy method used can be observed. A possible explanation for the increased sensitivity to SEM with the nozzle extension is the significantly larger boundary layer thickness (see Figure 8). We are investigating the use of different inflow generation methods [47, 56] which are less noisy and transition towards realistic turbulence faster.

Finally the effects of mesh refinement on the far-field noise are presented for the coarse mesh (90M), medium mesh (120M) and fine mesh (210M) in Figure 15. The surface triangulation chosen for this comparison has a slope of 0.10 and the radial flare starts at $y/D_j = 0.60$. All of the compared simulations are carried out without using SEM at the LES interface. The coarse mesh generally over predicts the noise spectra for low frequencies by around 4 dB. The peak observed in the coarse simulation at Strouhal numbers of around 4.5 are likely due to the delay in breaking down the quasi two-dimensional eddies to three-dimensional turbulence in the nozzle shear layer [9]. Good agreement for all mesh resolutions were achieved.

C. Jet Surface Interaction

The results in this section represent our first attempt in capturing the noise created by a jet flow near a surface shielding plate. The corresponding jet surface interaction tests were conducted at the Small Hot Jet Acoustic Rig (SHJAR), which is located in the Aeroacoustic Propulsion Laboratory (AAPL) at NASA Glenn Research Center [15, 16]. The specific configuration chosen for this study is a plate in $1.0D_j$ distance to the jet axis. The plate has a length of $8D_j$ and a width of $12D_j$. A sketch of the setup can be seen in Figure 2. Details of the SHJAR, the measurement techniques used to acquire the near-field and far-field data, and validation of experimental results are presented in Refs. [1, 17].

The mesh used is based on the medium CFD mesh from the isolated configuration and a plate mesh containing 130M grid points is added around the plate. For more details see section III. Due to the large streamwise and spanwise extent of the plate, this case is computationally very challenging as a sufficient mesh resolution has to be maintained over the whole plate in order to capture the shielding capability at higher frequencies. Considering that good results were achieved for the isolated round jet both for near-field and far-field with 120M grid points on the medium mesh the computational costs have more than doubled for the jet-surface interaction configuration.

1. Comparison to Experimental Data: Flow-Field and Near-Field

Figure 16 shows a general view of the flow field with a plate inserted at $z/D_j = -1.0$. The structures of the jet are visualized by the isocontour of the Q-criteria colored by the normalized streamwise velocity. The merging of the three-dimensional turbulent structures in the jet shear layer at the end of the potential core and the acoustic waves generated by the breakdown of the potential core and shear layer mixing are clearly illustrated. The scrubbing of the jet on the plate as a result of its close proximity can be clearly observed. It also appears that the off-track observer angles between 30° and 50° have stronger acoustic waves than the observer angles in the centerline plane. The experimental data published does not contain observer angles in the circumferential plane offset from the centerline for comparison. The effect of the plate shielding as well as acoustic waves generated at the trailing edge of the plate can clearly be observed in the streamwise cutting planes A through D as well as in the density gradient magnitude plot in sub-figure (b).

Figure 17 shows the qualitative comparison with an overall good agreement of the experimental PIV streamwise velocity statistics in the jet plume and the ZDES Mode III results. The centerline velocity is slightly larger in the simulation compared to the experiment. The corresponding centerline as well as lip-line velocity and turbulent kinetic energy profiles are presented in Figure 18 (a) and (b) respectively. It should be noted that reliable experimental PIV measurements are not available within $x/D_j < 0.5$ due to edge effects and lack of seeding homogeneity. Overall good agreement between measurement and simulations has been obtained. A slightly higher centerline velocity can be observed for $x/D_j > 12$. Similar findings are presented in Bres *et.al.* [6, 50] on their finer mesh, which had a slightly larger centerline velocity compared to experiments and their coarser simulation. The peak magnitude as well as location of the TKE along the centerline was well captured, however a small premature increase in TKE was observed. The difference in velocity at the lip line closer to the shielding plate ($y/D_j = -0.5$) and away from the plate ($y/D_j = 0.5$) has been captured very well in the simulation. However a slight over prediction of velocity until $x/D_j = 3$ has been

observed. A possible reason for this trend might be the mesh quality at this location. As the mesh is strongly clustered along the shear layer and stretches out towards the plate surface, the resolution might not be sufficient to capture the effects of the plate accurately in this region. A larger deviation from experimental results is observed in the lipline TKE values. The ZDES Mode III simulation grossly over-predicts the turbulent kinetic energy until around $x/D_j = 3$. This is caused by delay in transitioning towards realistic fully turbulent three-dimensional structures. These non-physical quasi two-dimensional structures (see also Figure 6 for the isolated configuration) contain too much energy at large scales and need to be broken down in the nozzle BL before they exit into the shear-layer. In order to improve this over-prediction, physical three-dimensional structures must be resolved in the nozzle boundary layer upstream of the exit (currently in RANS mode up to 0.1δ for ZDES Mode III). This can be accomplished by further improvements in the upstream mesh inside of the nozzle and by tripping the boundary layer to transition towards turbulence. As shown in a previous publication [12] utilizing a synthetic inflow turbulence generation method will reduce this over-prediction, however as shown in section IV.B this will result in an increase of the far-field noise for high frequencies. The investigation of various quieter inflow techniques is an ongoing effort within the group and will be reported in the future. For example Bres *et.al.* [50] showed that the lip-line RMS over-prediction at the nozzle exit can be completely removed by simply applying wall-modeled LES (WMLES) using a numerical scheme with almost no dissipation, an explicit sub-grid scale model and a locally refined mesh in the boundary layer. In their simulations, the flow naturally transitioned far upstream of the nozzle exit, and well-developed three-dimensional flow structures are observed within the nozzle. However the nozzle boundary layer in their simulation was significantly larger than the BL in our simulation. Even with the extended SMC000 geometry the convex nozzle shape right before the nozzle exit resulted in a thinning of the boundary layer towards the nozzle exit. Overall excellent agreement with experimental results have been observed for both lipline and centerline velocities and turbulent kinetic energy. The effects of the shielding plate on the lip-line profiles have been captured well, with a slight over-prediction of TKE in the initial shear-layer.

2. Comparison to Experimental Data: Far-Field

The same procedure as mentioned in the previous section was used for post-processing the far-field data in the jet-shielding case. In contrast to the axisymmetric jet, no averaging of circumferential observers can be performed, which makes it necessary to run the simulation over a longer time period for adequate statistical convergence of the predicted far-field noise spectrum. For this reason, the simulation was run for 120,000 iterations and window averaged over 25 windows with 50% overlap of comparable size instead of 5 windows for the isolated case. The Strouhal resolution is consistent with the one reported for the isolated case between $\Delta St_{window} = 0.02$. Hanning windowing was applied and the results were corrected to account for the energy loss from the windowing procedure.

Including even a simple flat plate in the simulation in order to assess the jet-shielding capabilities significantly increases the complexity of defining an appropriate FWH surface triangulation. For this reason, two permeable FWH surfaces have been constructed and are depicted in Figure 19. The main variation in the surfaces is the modification of the shape enclosing the plate surface. The cone intersecting the plate surface part is consistent with the one reported in the isolated case and has a slope of 0.10 and the starting point of the radial flare is at $y/D_j = 0.6$. First a tight surface triangulation has been created, which adds a straight section around the baseline surface triangulation connecting the circular wake triangulation mesh with the rectangular plate triangulation. In addition a looser surface has been created that would contain all acoustic waves propagating from the top of the jet towards each edge of the plate. In order to determine the number of points on the permeable surface triangulation, an automated surface mesh refinement tool has been developed which adds points to the triangulation based on underlying CFD mesh cell quality. The total amount of surface elements came down to around 600,000 triangles.

The propagation of a high-frequency acoustic wave approximated as a ray is depicted in a sketch for a tight FWH triangulation (a) and loose triangulation (b) in Figure 20. Given a tight surface triangulation and sufficient mesh resolution in order to propagate an acoustic wave all the way to the end of the plate, the wave would add a contribution to the FWH surface triangulation in three different locations. Two of those contributions (denoted as 1 and 2 in the sketch) would add up to the power spectral density value at the shielded side which would be canceled out by the third contribution (denoted as 3) thus not adding any noise to the shielded observers directly. For the loose surface triangulation only the reflected wave (denoted as 1 in sub-figure 20 (b)) would contribute to the FWH propagation procedure towards the shielded side. However in order for both of those methods to be accurate with minimal error, the mesh resolution requirements for the relatively long plate would be extremely large. Considering that a minimum of 9 points per wavelength are necessary for the WCNS scheme used in this paper, maintaining this grid resolution for a Strouhal number of 6 would add several hundred of millions of grid points to the simulation due to the large dimensions

of the plate. Note that for a full flight configuration, the dimensions of a given shielding element would be significantly smaller.

As this study reports our first attempt in predicting far-field noise from a jet shielding plate, a more economical approach has been chosen which only resolves around 4 points per wavelength towards the end of the plate for St=6. Hence we do not expect to match the experimental values for the high frequencies.

Figure 21 shows the comparison between the experimental measurements and the predictions from the ZDES Mode III simulation for the far-field power spectral density (PSD) 100D away from the nozzle exit for the observer angles $\Phi = 60^\circ, 90^\circ, 120^\circ, 150^\circ$ using the tight surface triangulation. Generally a good agreement is observed in the narrow-band spectrum for all observer angles. The peak Strouhal frequency, as well as the shielding capability, has been well captured in this simulation. For Strouhal numbers larger than 1.5 the power spectral density is over-predicted on the shielded side. This is expected, as the contributions to the shielded side on the tight permeable surface triangulation's are not adequately canceled out as a result of the numerical dissipation of the scheme (see Figure 20, contributions 1 and 2 are not canceled exactly by contribution 3 which results in a over-prediction on the shielded side). A similar but opposite effect is observed for the reflected side. The acoustic wave penetrating the surface triangulation after being reflected has been dissipated too much, resulting in a lower contribution to the noise spectra.

Figure 22 shows the noise spectra for a loose surface triangulation. The split is captured at the right Stouhal number and good agreement for the peak noise level is achieved. A stronger decay in the spectra for high frequencies can be observed as the mesh resolution is not sufficient enough towards the end of the plate. Waves propagating to the side of the loose surface triangulation are not fully captured anymore, resulting in a even stronger decay compared to the isolated round jet.

In conclusion, a good agreement for far-field noise spectra between the ZDES Mode III simulations and experimental dataset has been achieved. The capability of the ZDES Mode III method to accurately capture the split in sound spectra between shielded and reflected side has been demonstrated. Due to the large computational demands of resolving the shielding effects over the whole plate across the entire frequency range, a compromise had to be made between accuracy and feasibility. Currently a finer simulation is being carried out in order to gain better understanding of this problem.

The validated simulation database will also be used in the future to evaluate ways to predict shielding of a simple free jet by a plate using the LAVA Helmholtz solver which includes scattering effects. This simple and cost effective approach makes it possible to predict the shielding effects of the plate in a far more economical way without running additional simulations for different plate heights and designs.

V. Conclusion

The hybrid RANS/LES approach, within the LAVA framework, using structured curvilinear overlapping grids has been applied to the prediction of jet noise and compared to existing near-field PIV and far-field microphone data. A strong agreement in the prediction of the potential core length and centerline turbulent kinetic energy magnitude as well as location was observed for both the free-jet and jet-plate interaction case. Far-field acoustic predictions of the narrow band PSD compare well to experimental data in both shape and levels. The shielding effect of the plate was accurately captured for low to mid frequencies where the dominant noise levels are contained. Improvements in the prediction of sound spectra for higher frequencies require higher mesh resolution around the plate. To better capture the lip-line RMS and sideline PSD levels, improvements in the resolution of three dimensional turbulent structures inside the nozzle boundary layer are required. This can be achieved through finer mesh resolution in the axial and circumferential directions, as well as improvements in the modeling of the flow inside the nozzle. Many low fidelity engine exhaust noise prediction tools lack the capability to include nearby airframe surfaces. The simulations included in this work will help understand jet-surface interaction and thereby assist the development, improvement and validation of such tools. For canonical jet configurations without airframe interaction it is relatively straight forward to define a permeable Ffowcs Williams Hawkings surface in order to assess the noise created by the jet. However, including a plate makes this a non-trivial task. This work presents a first attempt towards systematically documenting the best practices for such flow configurations.

Acknowledgments

This work was partially funded by the Commercial Supersonics Technology (CST) project under the Advanced Air Vehicles Program (AAVP). We would like to thank our LAVA team members for countless fruitful discussions and all

the help. We would also like to thank Daniel Ingraham from NASA Glenn Research Center for valuable discussions during this work. Computer time has been provided by the NASA Advanced Supercomputing (NAS) facility at NASA Ames Research Center.

References

- [1] Brown, C., "Jet-Surface Interaction Test: Far-Field Noise Results," *Proceedings of the ASME Turbo Expo 2012, Copenhagen, Denmark*, 2012.
- [2] Pidboy, G., "Jet-Surface Interaction Test: Phased Array Noise Source Localization Results," *GT2012-69801*, 2012.
- [3] Welge, H., Bonet, J., Magee, T., Tompkins, D., Brit, T., Nelson, C., Miller, G., Stenson, D., Staubach, J., and Bala, N., "N plus 3 Advanced Concept Studies for Supersonic Commerical Transport Aircraft Entering Servie," *NASA/CR-2011-217084*, 2011.
- [4] Kim, H., "Distributed Propulsion Vehicles," *ICAS*, 2010.
- [5] Bres, G., Nichols, J., Lele, S., and Ham, F., "Towards Best Practices for Jet Noise Predictions with Unstructured Large Eddy Simulations," *42nd AIAA Fluid Dynamics Conference, New Orleans, Louisiana*, 2012. AIAA-2012-2965.
- [6] Bres, G., Jordan, P., Jaunet, V., Ke Rallic, M., Cavalieri, A., Towne, A., Lele, S., Colonius, T., and Schmidt, O., "Importance of nozzle-exit boundary-layer state in subsonic turbulent jets," *Journal of Fluid Mechanics*, Vol. 851, 2018, pp. 83–124.
- [7] Ingraham, D., and Bridges, J., "Validating a Monotonically-Integrated Large Eddy Simulation Code for Subsonic Jet Acoustics," *55th AIAA Aerospace Sciences Meeting, Grapevine, Texas*, 2017. AIAA-2017-0456.
- [8] Jordan, P., and Colonius, T., "Wave Packets and Turbulent Jet Noise," *Annual Review of Fluid Mechanics*, Vol. 45, 2013, pp. 173–195.
- [9] Bodony, D., and Lele, S., "Current Status of Jet Noise Predictions Using Large-Eddy Simulation," *AIAA Journal*, Vol. 46, No. 2, 2008, pp. 364–380.
- [10] Housman, J., Stich, G., and Kiris, C., "Predictions of Slat Noise from the 30P30N at High Angles of Attack using Zonal Hybrid RANS-LES," *AIAA/CEAS Aeroacoustics Conference*, 2019.
- [11] Barad, M., Kocheemoolayil, J., and Kiris, C., "Lattice Boltzmann and Navier-Stokes Cartesian CFD Approaches for Airframe Noise Predictions," *AIAA Aviation Forum*, Vol. 23, 2017.
- [12] Housman, J., and Kiris, C., "Structured Overlapping Grid Simulations of Contra-Rotating Open Rotor Noise," *54th AIAA Aerospace Sciences Meeting*, 2016. AIAA-2016-0814.
- [13] Stich, G.-D., Housman, J., Kocheemoolayil, J., Barad, M., and Kiris, C., "Application of Lattice Boltzmann and Navier-Stokes Methods to NASA's Wall Mounted Hump," *AIAA Aviation Forum, Atlanta, Georgia*, 2018.
- [14] Housman, J., Stich, G., and Kiris, C., "Jet Noise Prediction using Hybrid RANS/LES with Structured Overset Grids," *23rd AIAA/CEAS Aeroacoustic Conference, Denver, Colorado*, 2017. AIAA-2017-3213.
- [15] Brown, C., and Bridges, J., "Small Hot Jet Acoustic Rig Validation," Technical Memorandum NASA-TM-2006-214234, National Aeronautics and Space Administration, 2006.
- [16] Bridges, J., and Brown, C., "Validation of the Small Hot Jet Acoustic Rig for Jet Noise Research," Tech. Rep. AIAA 2005-2846, AIAA, 2005.
- [17] Brown, C., and Wernet, M., "Jet-Surface Interaction Test: Flow Measurement Results," *20th AIAA/CEAS Aeroacoustics Conference*, 2014. AIAA 2014-3198.
- [18] Kiris, C., Housman, J., Barad, M., Brehm, C., Sozer, E., and Moini-Yekta, S., "Computational Framework for Launch, Ascent, and Vehicle Aerodynamics (LAVA)," *Aerospace Science and Technology*, Vol. 55, 2016, pp. 189–219.
- [19] Steger, J., and Benek, J., "On the Use of Composite Grid Schemes in Computational Aerodynamics," Technical Memorandum 88372, NASA, 1986.
- [20] Chan, W., "Developments in Strategies and Software Tools for Overset Structured Grid Generation and Connectivity," *20th AIAA Computational Fluid Dynamics Conference, Honolulu, Hawaii*, 2011. AIAA-2011-3051.

- [21] Spalart, S., and Allmaras, S., “A One-Equation Turbulence Model for Aerodynamic Flows,” *30th Aerospace Sciences Meeting and Exhibit, Reno, NV*, 1992. AIAA-92-0439.
- [22] Brehm, C., Housman, J., Kiris, C., and Hutcheson, F., “Noise Characteristics of a Four-Jet Impingement Device Inside a Broadband Engine Noise Simulator,” *21st AIAA/CEAS Aeroacoustics Conference, Dallas, Texas*, 2015. AIAA-2015-2211.
- [23] Housman, J., and Kiris, C., “Slat Noise Predictions using Higher-Order Finite-Difference Methods on Overset Grids,” *22nd AIAA/CEAS Aeroacoustic Conference, Lyon, France*, 2016. AIAA-2016-2963.
- [24] Brehm, C., Housman, J., and Kiris, C., “Noise Generation Mechanisms for a supersonic jet impinging on an inclined plate,” *Journal of Fluid Mechanics*, Vol. 797, 2016, pp. 802–850.
- [25] Brehm, C., Barad, M., Housman, J., and Kiris, C., “A Comparison of Higher-Order Finite-Difference Shock Capturing Schemes,” *Computers & Fluids*, Vol. 122, 2015, pp. 184–208.
- [26] Shu, C.-W., “High Order Weighted Essentially Nonoscillatory Schemes for Convection Dominated Problems,” *SIAM Review*, Vol. 51, No. 1, 2009, pp. 92–126.
- [27] Deng, X., and H., Z., “Developing High-Order Weighted Compact Nonlinear Schemes,” *Journal of Computational Physics*, Vol. 165, 2000, pp. 22–44.
- [28] Vinokur, M., and Yee, H., “Extension of Efficient Low Dissipation High Order Schemes for 3-D Curvilinear Moving Grids,” *Frontiers of Computational Fluid Dynamics*, World Scientific, 2002, pp. 129–163. Edited by D. A. Caughey and M. M. Hafez.
- [29] Deng, X., Mao, M., Tu, G., Liu, H., and Zhang, H., “Geometric Conservation Law and Applications to High-Order Finite Difference Schemes with Stationary Grids,” *Journal of Computational Physics*, Vol. 230, 2011, pp. 1100–1115.
- [30] Housman, J., Kiris, C., and Hafez, M., “Preconditioned methods for simulations of low speed compressible flows,” *Computers & Fluids*, Vol. 38, No. 7, 2009, pp. 1411–1423.
- [31] Housman, J., Kiris, C., and Hafez, M., “Time-Derivative Preconditioning Methods for Multicomponent Flows - Part I: Riemann Problems,” *Journal of Applied Mechanics*, Vol. 76, No. 2, 2009.
- [32] Housman, J., Kiris, C., and Hafez, M., “Time-Derivative Preconditioning Methods for Multicomponent Flows - Part II: Two-Dimensional Applications,” *Journal of Applied Mechanics*, Vol. 76, No. 3, 2009.
- [33] Deng, X., Mao, M., Jiang, Y., and Liu, H., “New High-Order Hybrid Cell-Edge and Cell-Node Weighted Compact Nonlinear Schemes,” *20th AIAA Computational Fluid Dynamics Conference, Honolulu, Hawaii*, 2011. AIAA-2011-3857.
- [34] Nonomura, T., and Fujii, K., “Robust Explicit Formulation of Weighted Compact Nonlinear Scheme,” *Computers & Fluids*, Vol. 85, 2013, pp. 8–18.
- [35] Spalart, S. R., Jou, W.-H., Strelets, M., and Allmaras, S. R., “Comments on the feasibility of LES for wings, and on a hybrid RANS/LES approach,” *First AFOSR international conference on DNS/LES, Ruston, Louisiana*, 1997. Greyden Press.
- [36] Strelets, M., “Detached eddy simulation of massively separated flows,” *39th Aerospace Sciences Meeting and Exhibit, Reno, Nevada*, 2001. AIAA-2001-0879.
- [37] Spalart, P., Deck, S., Shur, M., Squires, K., Strelets, M., and Travin, A., “A New Version of Detached-Eddy Simulation, Resistant to Ambiguous Grid Densities,” *Theoretical and Computational Fluid Dynamics*, Vol. 20, 2006, pp. 181–195.
- [38] Shur, M., Spalart, P. R., Strelets, M., and Travin, A., “A Hybrid RANS-LES Approach with Delayed-DES and Wall-Modelled LES Capabilities,” *International Journal of Heat and Fluid Flow*, Vol. 29, 2008, pp. 1638–1649.
- [39] Spalart, P. R., “Detached-Eddy Simulation,” *Annual Review Fluid Mechanics*, Vol. 41, 2009, pp. 181–202.
- [40] Caruelle, B., and Ducros, F., “Detached-Eddy Simulations of Attached and Detached Boundary Layers,” *International Journal of Computational Fluid Dynamics*, Vol. 17, 2003, pp. 433–451.
- [41] Ashton, N., West, A., and Mendonca, F., “Flow Dynamics Past a 30P30N Three-Element Airfoil Using Improved Delayed Detached-Eddy Simulation,” *AIAA Journal*, Vol. 54, No. 11, 2016, pp. 3657–3667.
- [42] Deck, S., “Numerical simulation of transonic buffeting over a supercritical airfoil,” *AIAA Journal*, Vol. 43, 2005, pp. 1556–1566.
- [43] Deck, S., “Zonal-detached eddy simulation of the flow around a high-lift configuration,” *AIAA Journal*, Vol. 43, 2005, pp. 2372–2384.

- [44] Deck, S., "Recent Improvements in the Zonal Detached-Eddy Simulation (ZDES) Formulation," *Theoretical and Computational Fluid Dynamics*, Vol. 26, 2012, pp. 523–550.
- [45] Eastwood, S., Xia, H., and Tucker, P., "Large-Eddy Simulation of Complex Geometry Jets," *Journal of Propulsion and Power*, Vol. 28, No. 2, 2012, pp. 235–245.
- [46] Zhu, H., Fu, S., Shi, L., and Wang, Z., "A Hybrid RANS-Implicit LES Approach for the High-Order FR/CPR Method," *54th AIAA Aerospace Sciences Meeting, San Diego, Ca.*, 2016. AIAA-2016-1599.
- [47] Deck, S., Weiss, P., Pamies, M., and Garnier, E., "Zonal Detached Eddy Simulation of a spatially developing flat plate turbulent boundary layer," *Computers and Fluids*, Vol. 48, 2011, pp. 1–15.
- [48] Deck, S., Renard, N., Laraufie, R., and Sagaut, P., "Zonal detached eddy Simulation (ZDES) of a spatially developing flat plate turbulent boundary layer over the Reynolds number range $3150 \leq Re_\theta \leq 14000$," *Physics of Fluids*, Vol. 26, 2014.
- [49] Renard, N., and Deck, S., "Improvements in Zonal Detached Eddy Simulation for Wall Modeled Large Eddy Simulation," *AIAA Journal*, Vol. 53, No. 11, 2015.
- [50] Bres, G., Nichols, J., Lele, S., and Ham, F., "Large Eddy Simulation for Jet Noise: the Importance of Getting the Boundary Layer Right," *21st AIAA/CEAS Aeroacoustics Conference, Dallas, Texas*, 2015. AIAA-2015-2535.
- [51] Uzun, A., and Hussaini, M. Y., "Investigation of High Frequency Noise Generation in the Near-Nozzle Region of a Jet Using Large Eddy Simulation," *Theoretical and Computational Fluid Dynamics*, Vol. 21, 2007, pp. 291–321.
- [52] Aikens, K., Dhamankar, N., Martha, C., Situ, Y., Blaisdell, G., Lyrintzis, A., and Li, Z., "Equilibrium Wall Model for Large Eddy Simulations of Jets for Aeroacoustics," *52nd AIAA Aerospace Sciences Meeting, National Harbor, Maryland*, 2014. AIAA-2014-0180.
- [53] Aikens, K., Blaisdell, G., and Lyrintzis, A., "Analysis of Converging-Diverging Beveled Nozzle Jets Using Large Eddy Simulation with a Wall Model," *53rd AIAA Aerospace Sciences Meeting, Kissimmee, Florida*, 2015. AIAA-2015-0509.
- [54] Jarrin, N., Benhamadouche, S., Laurence, D., and Prosser, R., "A Synthetic-Eddy-Method for Generating Inflow Conditions for Large-Eddy Simulations," *International Journal of Heat and Fluid Flow*, Vol. 27, 2006, pp. 585–593.
- [55] Jarrin, N., Prosser, R., Uribe, J.-C., Benhamadouche, S., and Laurence, D., "Reconstruction of Turbulent Fluctuations for Hybrid RANS/LES simulations using a Synthetic-Eddy Method," *International Journal of Heat and Fluid Flow*, Vol. 30, 2009, pp. 435–442.
- [56] Shur, M., Spalart, P., Strelets, M., and Travin, A., "Synthetic Turbulence Generators for RANS-LES Interfaces in Zonal Simulations of Aerodynamic and Aeroacoustic Problems," *Flow Turbulence and Combustion*, Vol. 93, 2014, pp. 63–92.
- [57] Pope, S., "A more general effective-viscosity hypothesis," *Journal of Fluid Mechanics*, Vol. 72, 1975, pp. 331–340.
- [58] Bogey, C., and Marsden, O., "A Study of the Grid Dependence of the Flow Field and Noise of Subsonic Jets," *54th AIAA Aerospace Science Meeting, San Diego, Ca*, 2016. AIAA-2016-0261.
- [59] Shur, M., Spalart, P. R., and Strelets, M., "Noise prediction for increasingly complex jets, Part 1 Methods and Tests," *International Journal of Aeroacoustics*, Vol. 4, 2005, pp. 213–246.
- [60] Shur, M., Spalart, P. R., and Strelets, M., "Noise prediction for increasingly complex jets, Part 2 Applications," *International Journal of Aeroacoustics*, Vol. 4, 2005, pp. 247–266.
- [61] Georgiadis, N., Rizzetta, D., and Fureby, C., "Large-Eddy Simulation: Current Capabilities, Recommended Practices, and Future Research," *47th AIAA Aerospace Sciences Meeting, Orlando, Florida*, 2009. AIAA-2008-948.
- [62] Larsson, J., Kawai, S., Bodart, J., and Bermejo-Moreno, I., "Large Eddy Simulation with Modeled Wall-Stress: Recent Progress and Future Directions," *J-STAGE*, 2015.
- [63] Tam, C., Viswanathan, K., Ahuja, K., and Panda, J., "The sources of jet noise: experimental evidence," *Journal of Fluid Mechanics*, Vol. 615, 2008, pp. 253–292.
- [64] Tam, C., and Burton, D., "Sound generated by instability waves of supersonic flows. Part 1. Two-dimensional mixing layers." *Journal of Fluid Mechanics*, Vol. 138, 1984, pp. 249–272.

- [65] Bridges, J., and Wernet, M., “The NASA Subsonic Jet Particle Image Velocimetry (PIV) Dataset,” Technical Memorandum NASA-TM-2011-216807, National Aeronautics and Space Administration, 2011.
- [66] Slotnick, J. e. a., “CFD Vision 2030 Study: A Path to Revolutionary Computational Aerosciences,” *NASA Technical Report*, 2014. NASA/CR-2014-218178.
- [67] Bogey, C., Bailly, C., and Juve, D., “Investigation of Downstream and Sideline Subsonic Jet Noise Using Large Eddy Simulation,” *Theor. Comput. Fluid Dyn.*, Vol. 20, 2006, pp. 23–40.
- [68] Bogey, C., and Bailly, C., “Influence of nozzle-exit boundary-layer conditions on the flow and acoustic fields of initial laminar jets,” *Journal of Fluid Mechanics*, Vol. 10, 2010, pp. 507–538.
- [69] Mendez, S., Shoeybi, M., Sharma, A., Ham, F., Lele, S., and Moin, P., “Large-Eddy Simulations of Perfectly-Expanded Supersonic Jets: Quality Assessment and Validation,” *48th AIAA Aerospace Sciences Meeting, Orlando, Florida*, 2010. AIAA-2010-271.
- [70] Rahier, G., Prieru, J., Vuillot, F., and Biancherin, A., “Investigation of integral surface formulations of acoustic predictions of hot jets starting from unsteady aerodynamic simulations,” 2003. AIAA-2003-3164.
- [71] Lockard, D., “A Comparison of Ffowcs Williams-Hawkins Solvers for Airframe Noise Applications,” *8th AIAA/CEAS Aeroacoustics Conference & Exhibit, Breckenridge, Colorado*, 2002. AIAA-2002-2580.
- [72] Spalart, P. R., and Shur, M., “Variants of the Ffowcs Williams-Hawkins Equation and their Coupling with Simulations of Hot Jets,” *International Journal of Aeroacoustics*, Vol. 8, No. 5, 2009, pp. 477–492.
- [73] Mendez, S., Shoeybi, M., Lele, S., and Moin, P., “On the use of the Ffowcs Williams-Hawkins Equation to Predict Far-Field Jet Noise from Large Eddy-Simulations,” *International Journal of Aeroacoustics*, Vol. 12, 2013.
- [74] Zaman, K., “Asymptotic spreading rate of initially compressible jets - experiment and analysis,” *Physics of Fluids*, Vol. 10, 1998, pp. 2652–2660.
- [75] Cadieux, F., Barad, M., and Kiris, C., “A High-Order Kinetic Energy Conserving Scheme for Compressible Large-Eddy Simulation,” *Tenth International Conference on Computational Fluid Dynamics (ICCFD10)*, 2018. ICCFD10-2018-100.



Fig. 2 (a) Picture of the Small Hot Jet Acoustic Rig (SHJAR) in acoustic configuration with 24 microphones centered around the nozzle exit [1]. (b) SMC000 round convergent nozzle used in this study. Drill holes for mounting the nozzle have not been considered in the CFD simulation to simplify the meshing. The nozzle has an exit diameter of 2 inch and a 12 inch straight section between the initial contraction and the nozzle. (bottom) nozzle interior, (top) nozzle exterior.

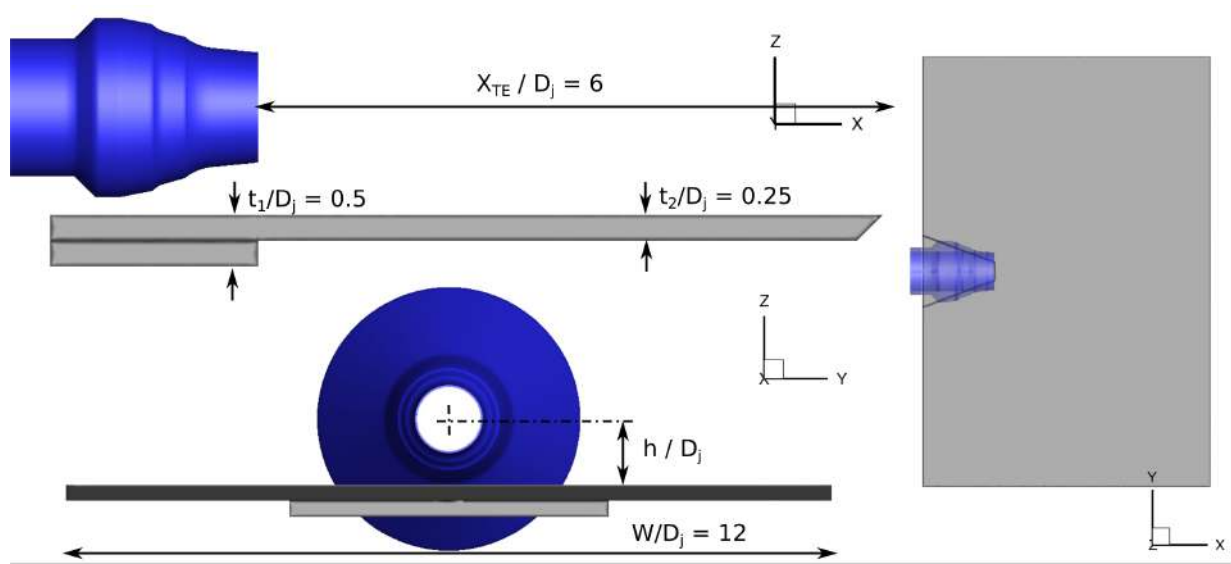


Fig. 3 Schematic showing the SMC000 configuration including the jet-shielding plate. Configuration considered in this study has a plate length of $8D_j$, a plate width of $12D_j$ and a distance of $h/D_j = 1$.

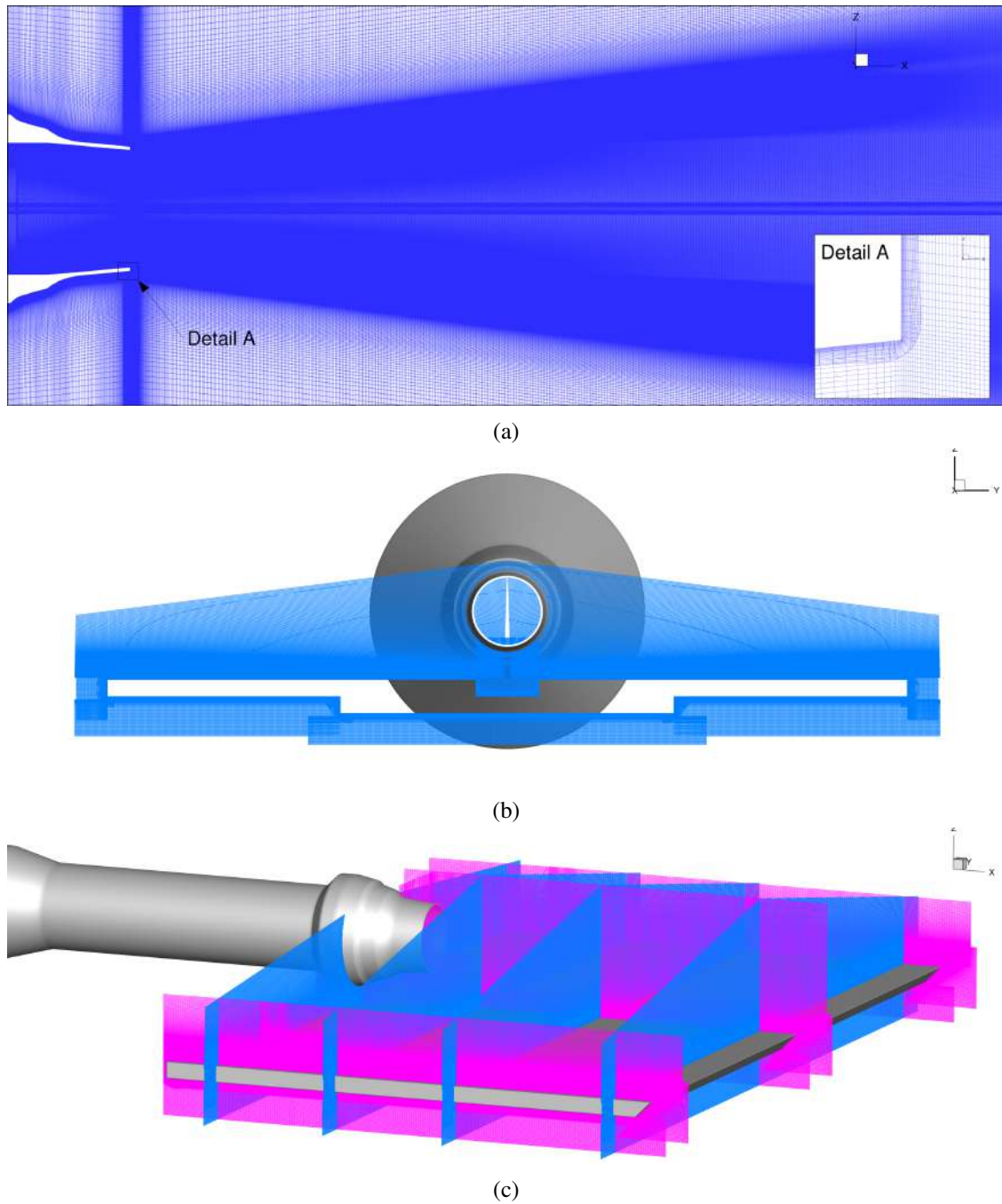
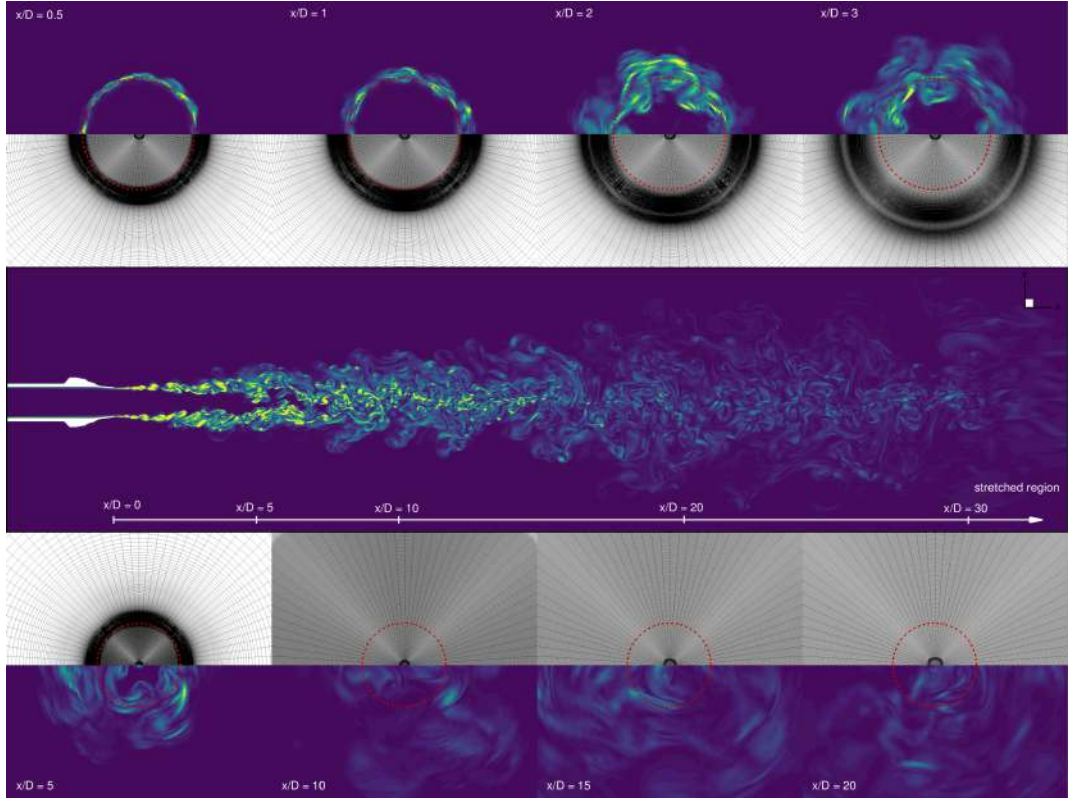
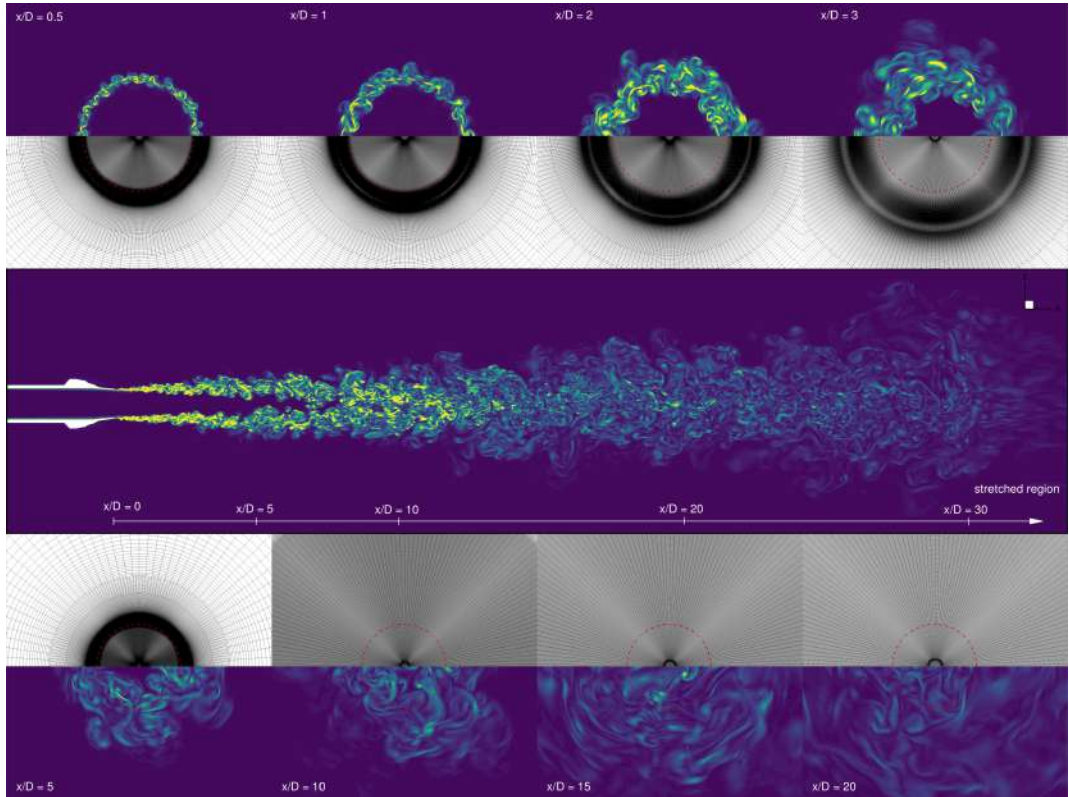


Fig. 4 (a) A cutting plane shown for the fine isolated mesh through the jet centerline on the structured overlapping grid system. Detail A shows overset lip mesh in RANS region. (b) slice at $x/D_j = -0.05$ of added plate mesh (c) different streamwise and spanwise cuts through plate mesh

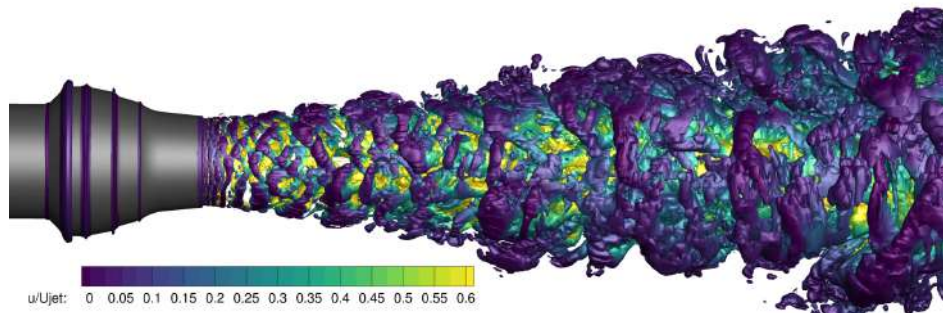


(a) isolated coarse mesh (90M)

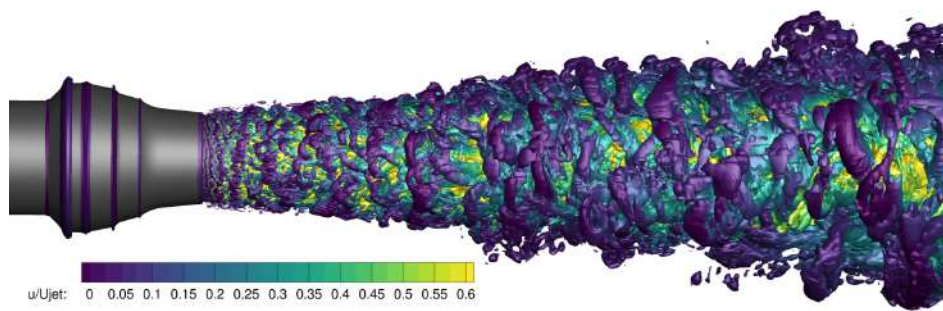


(b) isolated fine mesh (210M)

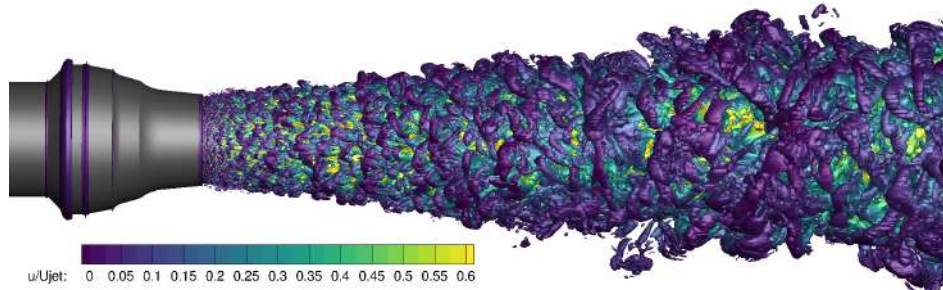
Fig. 5 Instantaneous vorticity magnitude for isolated isothermal ideally-expanded jet. Top and bottom sub-figures show cross-flow cuts at eight different streamwise locations. Dashed red line depicts the the nozzle exit lip-line at 2inch diameter. The sub-figures also partially contain the mesh refinement in circumferential direction.



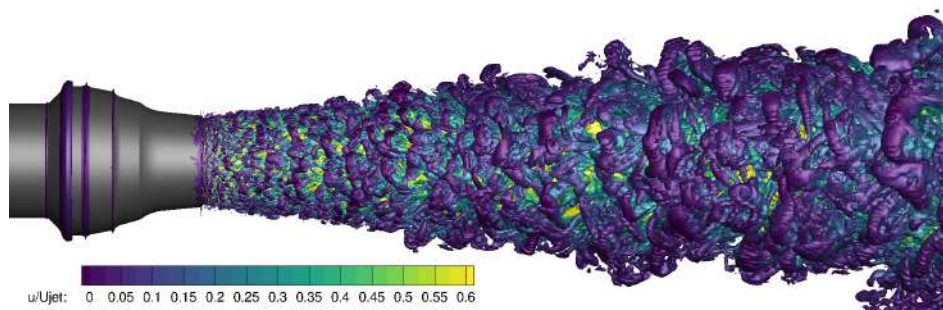
(a) coarse mesh (90M) - no SEM



(b) medium mesh (120M) - no SEM

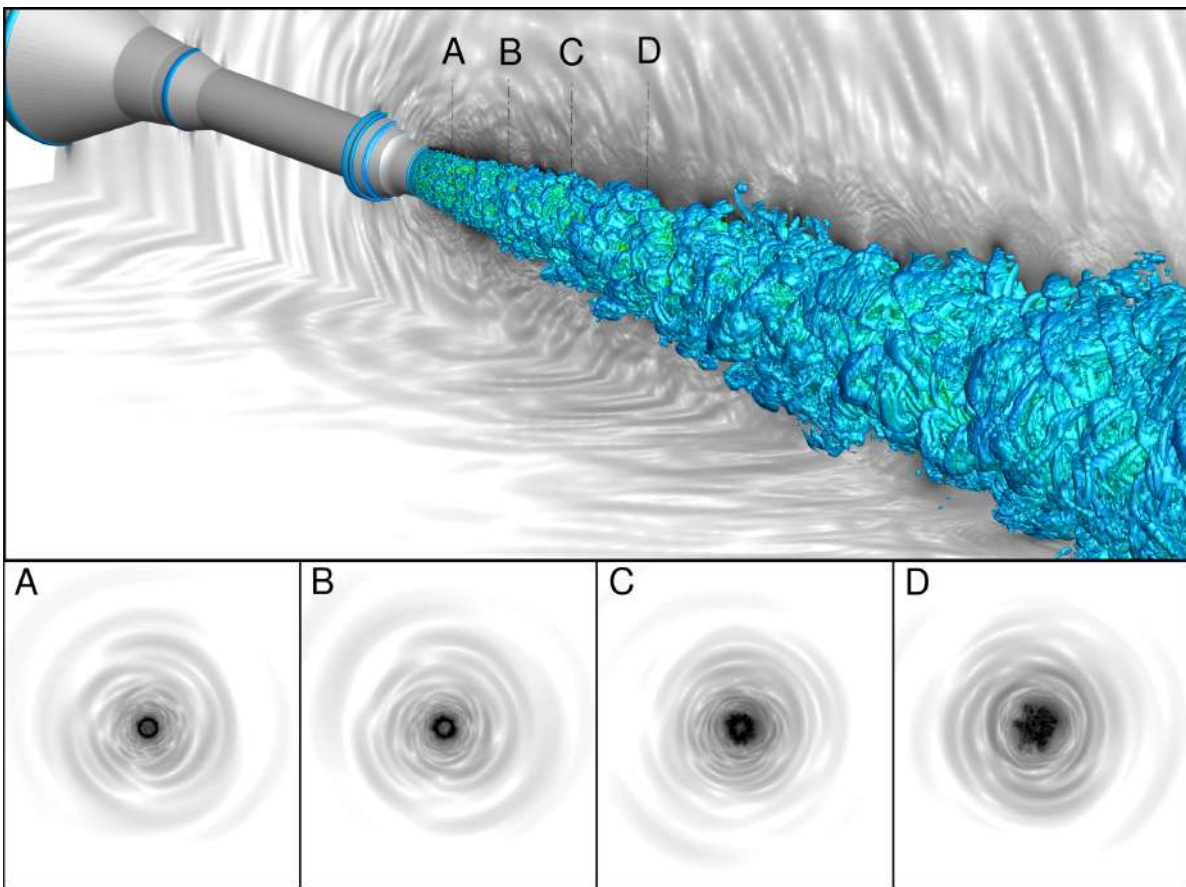


(c) fine mesh (210M) - no SEM

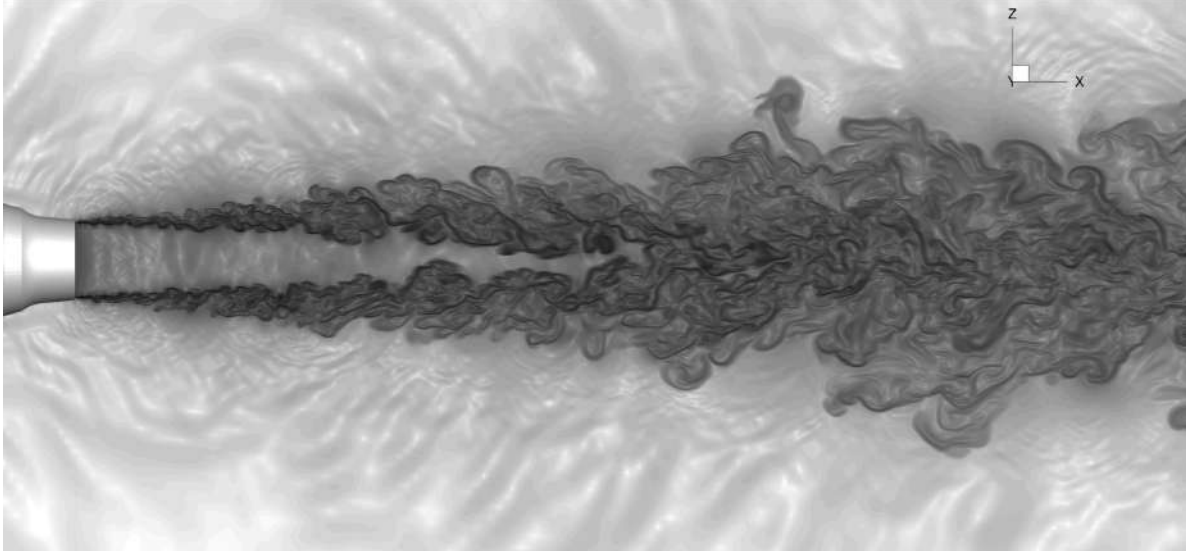


(d) fine mesh (210M) - SEM

Fig. 6 Comparison of iso-contour of Q-criteria colored by normalized axial velocity for three different mesh resolution. Sub-figures (c) and (d) show comparison of the use of SEM method using the same fine mesh resolution.



(a) Instantaneous Q-criteria colored by axial velocity and pressure gradient magnitude at different streamwise slices



(b) Instantaneous magnitude of the density gradient

Fig. 7 Instantaneous flow field images of (a) Q-criteria colored by normalized axial velocity and pressure gradient magnitude at a plane through the centerline and at $y/D_j = -1.5$. (b) magnitude of density gradient showing the resolved three-dimensional turbulent structures and the acoustic waves propagating to the far-field on the medium grid (120M).

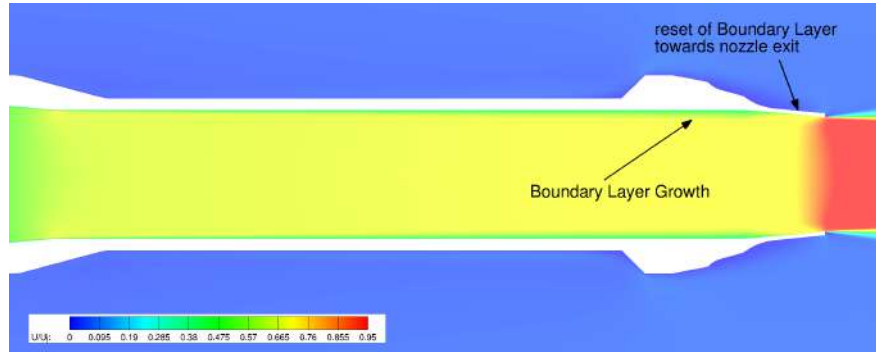


Fig. 8 Normalized axial velocity contour plot from RANS simulation on fine mesh (210M). Growth of boundary layer inside of the nozzle due to 12" straight section and reset of boundary layer at convergent nozzle part displayed.

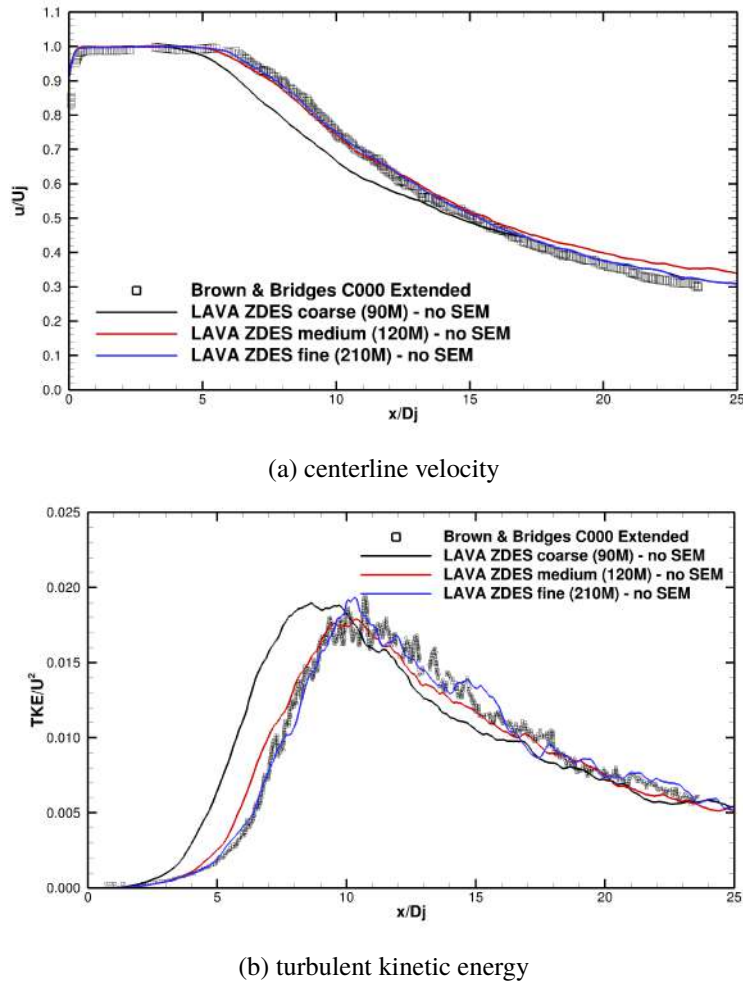


Fig. 9 Time-averaged centerline velocity and turbulent kinetic energy (TKE) for isolated baseline configuration on coarse (90M), medium (120M) and fine (210M) mesh normalized by jet diameter (x/D_j) and centerline velocity (U_j).

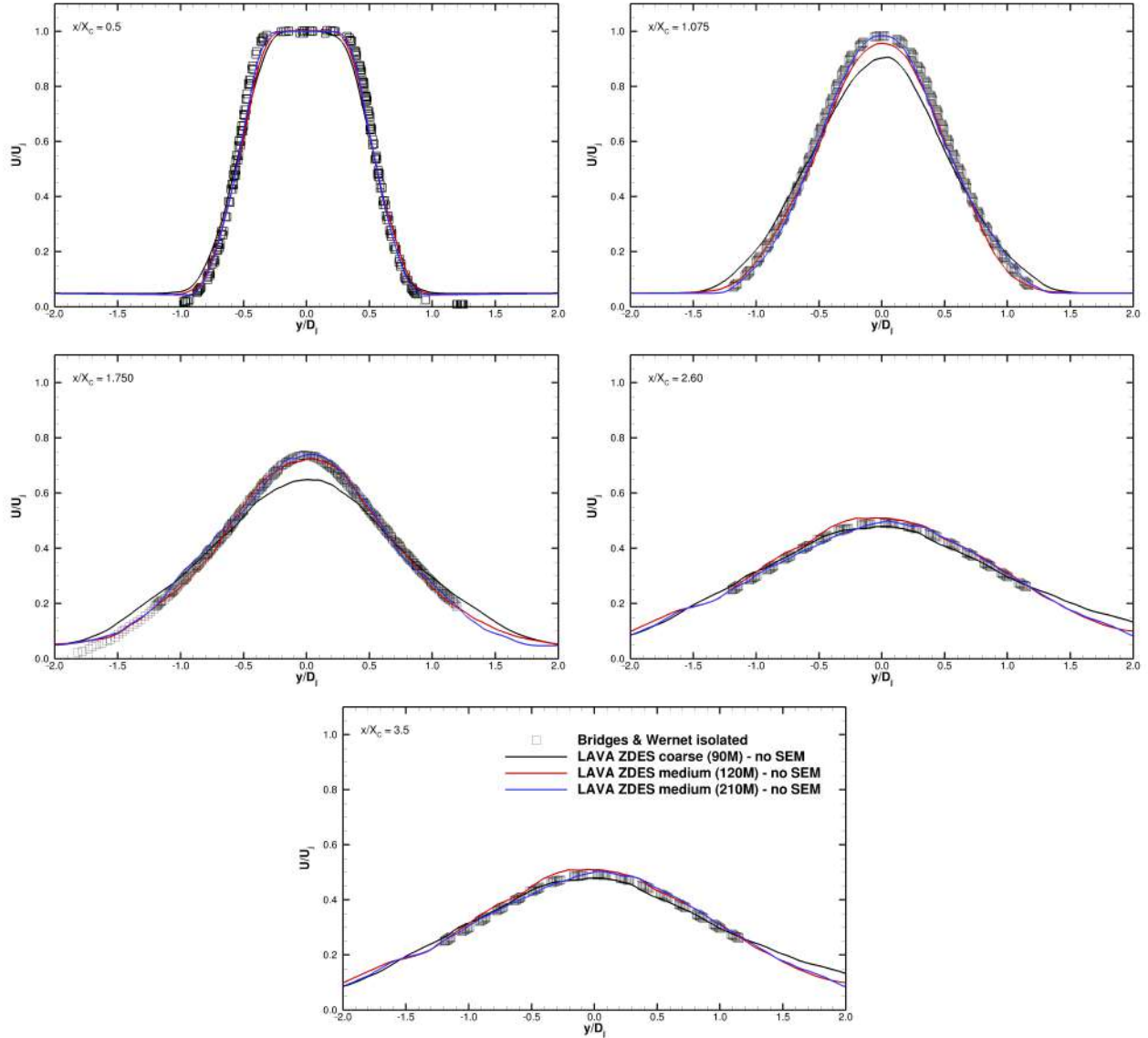


Fig. 10 Axial normalized velocity at four axial locations normalized by length of potential core $X_C = 5.9$ for the coarse (90M), medium (120M) and fine (210M) isolated mesh.

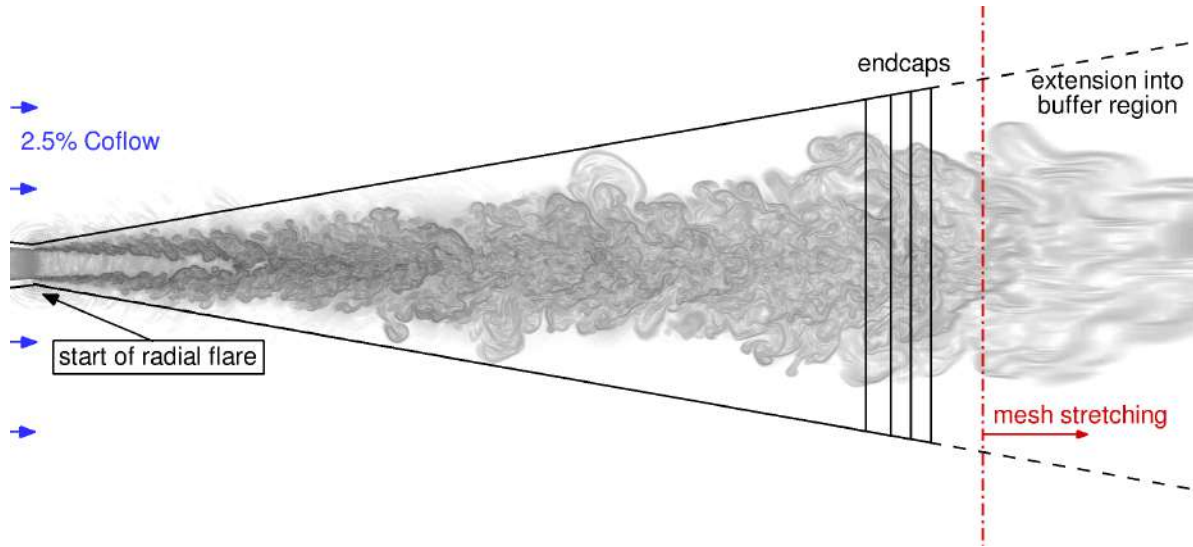


Fig. 11 Outline of FWH surface placement with end-caps between $25D$ and $30D$ (solid line) and open outflow disk FWH surface extended into the outflow buffer region (dashed line). Density gradient of magnitude displayed on the centerline plane for the fine CFD mesh. (Number of end-caps has been reduced from 25 to 4 in this sketch for displaying purposes)

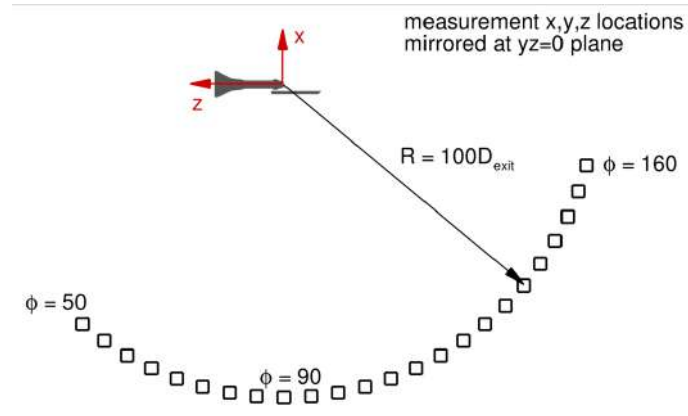


Fig. 12 Schematic of microphone array location for shielded data in $100D_j$ away from the nozzle exit. Microphone array mirrored at yz -plane for reflected microphone array. For isolated configuration microphone array at each observer rotated in plane and averaged over 360 observers per angle Φ .

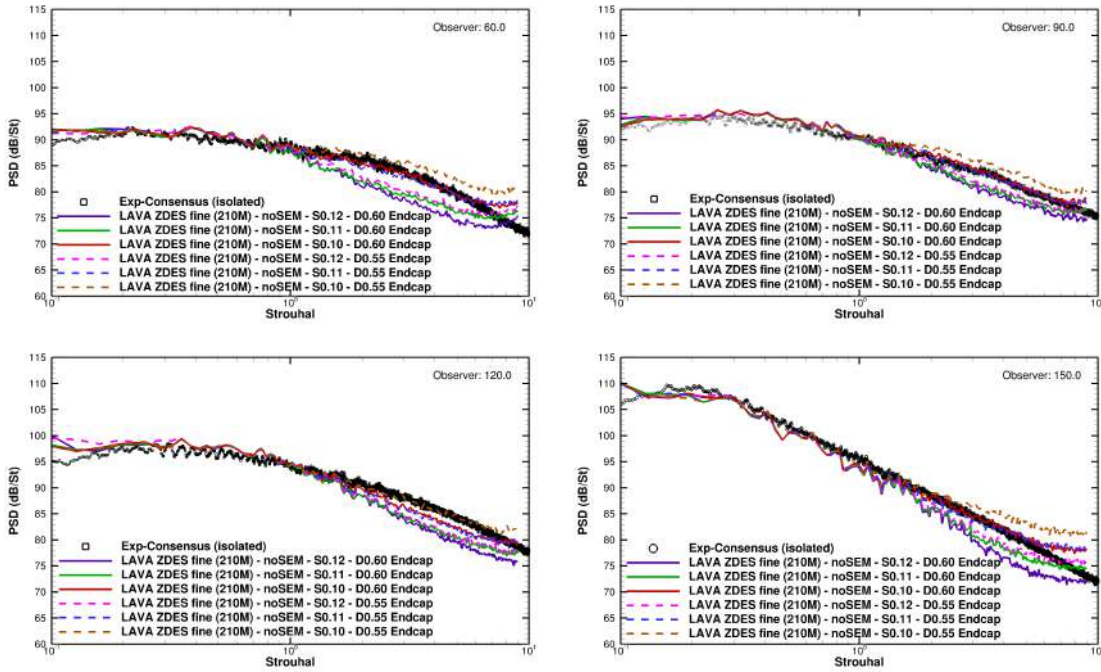


Fig. 13 Comparison of noise spectra between experimental consensus and ZDES Mode III at $100D_j$ for observer angles $\Phi = 60, 90, 120, 150$. FWH surface triangulation follows geometry with constant offset until nozzle exit and flares out with slope angles 0.10, 0.11 and 0.12. Start of flare of FWH surface $y/D_j = 0.5$ for solid lines and $y/D_j = 0.55$ for dashed lines.

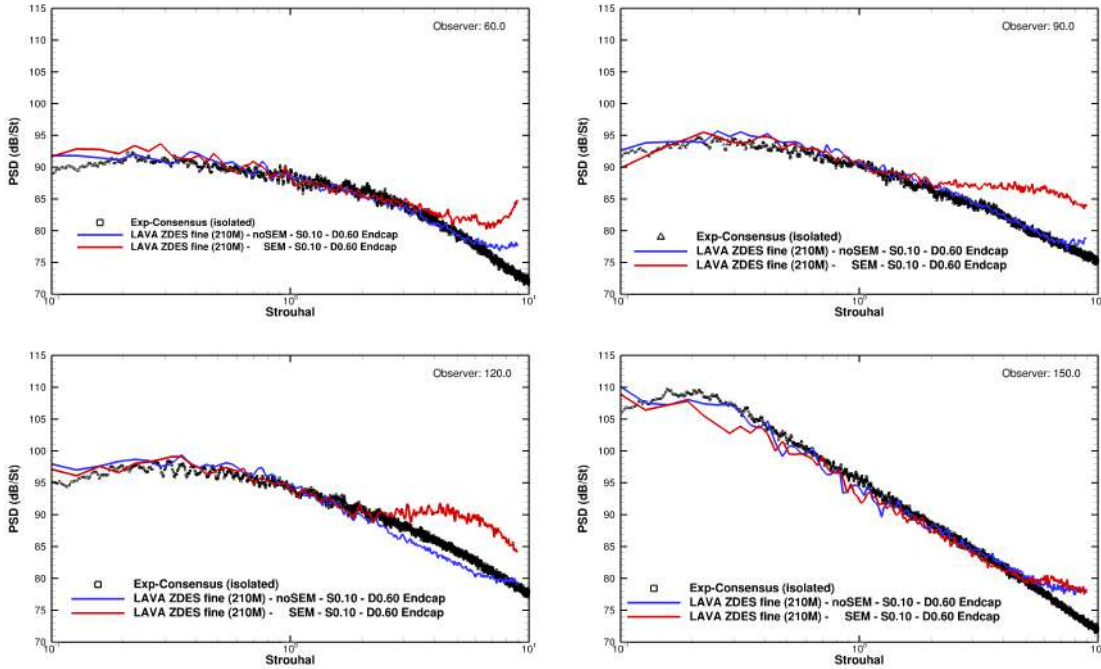


Fig. 14 Comparison of noise spectra between experimental consensus and ZDES Mode III at $100D_j$. Influence of inflow turbulence on far-field PSD on fine mesh (210M). Start radial flare of FWH surface $y/D_j = 0.6$ and slope 0.10.

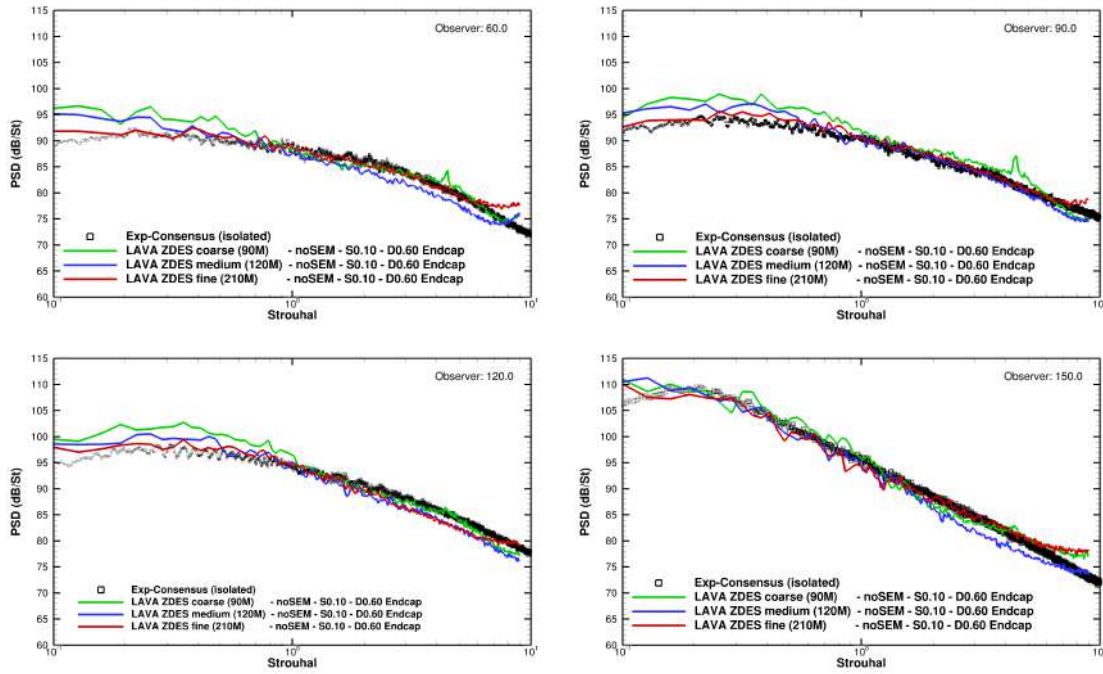
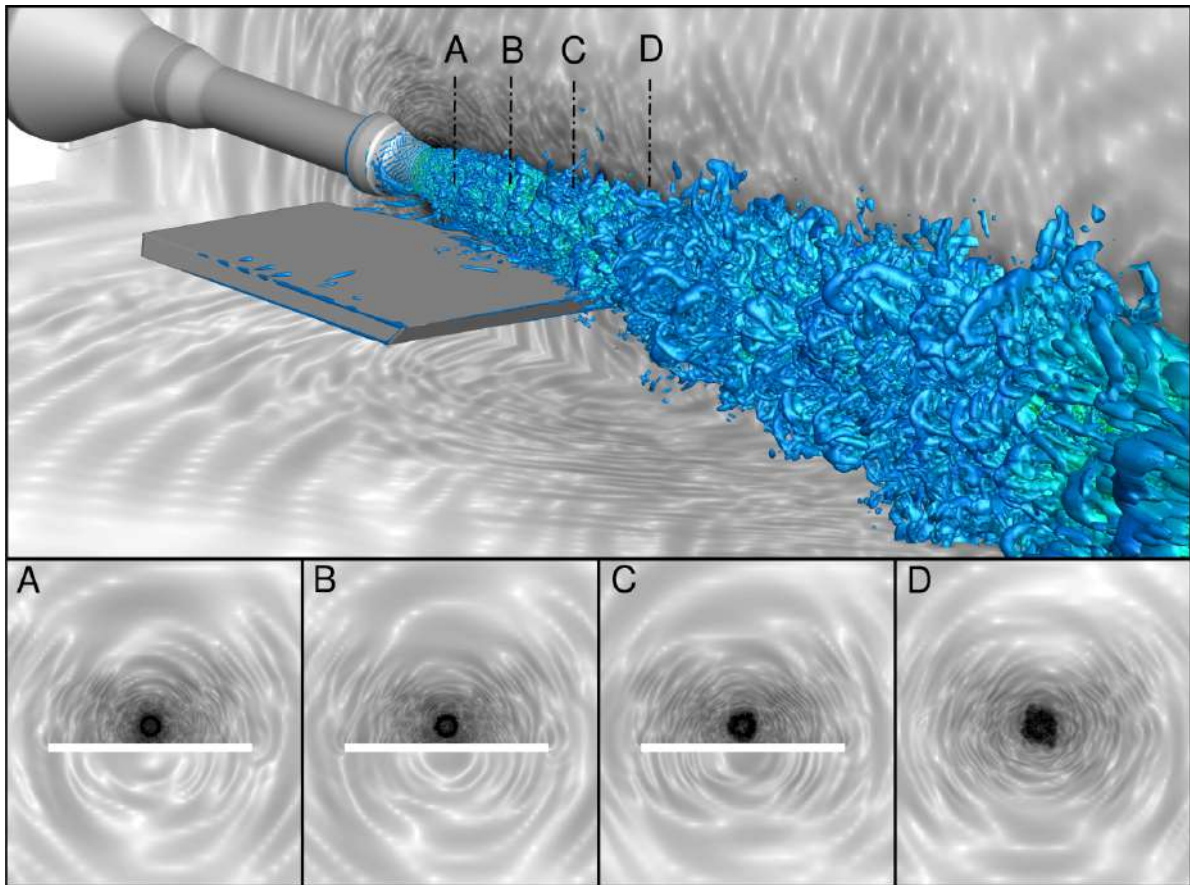
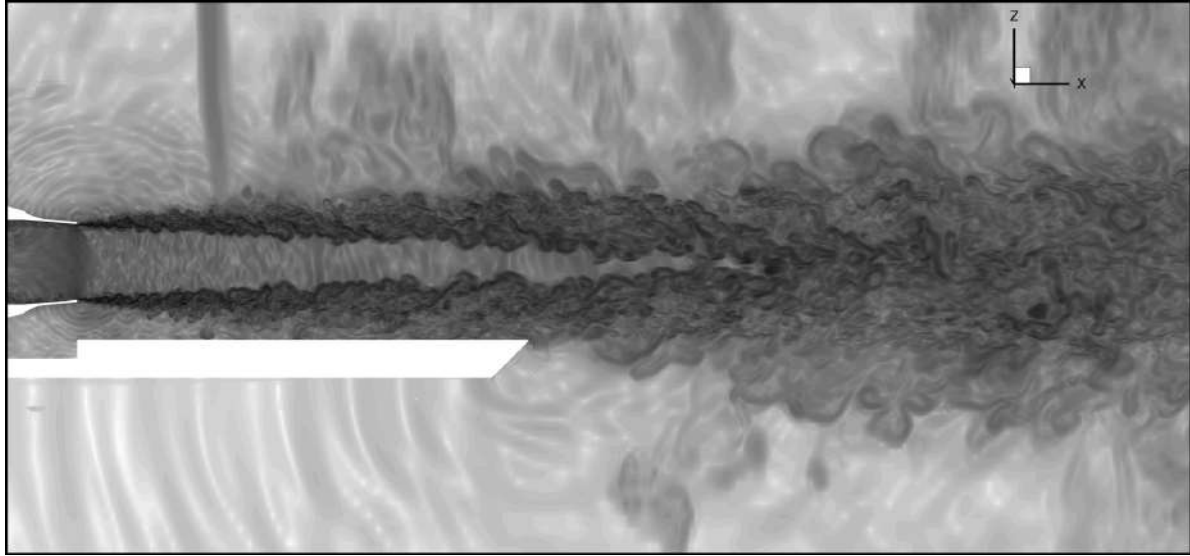


Fig. 15 Comparison of noise spectra between experimental consensus and ZDES Mode III at $100D_j$. Coarse mesh (90M), medium mesh (120M) and fine mesh (210M), all cases compared do not use SEM at the inflow. Start radial flare of FWH surface $y/D_j = 0.6$ and slope 0.10.



(a) Instantaneous Q-criteria colored by normalized axial velocity and pressure gradient magnitude at different streamwise slices



(b) Instantaneous magnitude of the density gradient

Fig. 16 Instantaneous flow field images of (a) Q-criteria colored by normalized axial velocity and pressure gradient magnitude at a plane through the centerline and at $y/D_j = -1.5$. (b) magnitude of density gradient showing the resolved three-dimensional turbulent structures and the acoustic waves propagating to the far-field on plate mesh (250M).

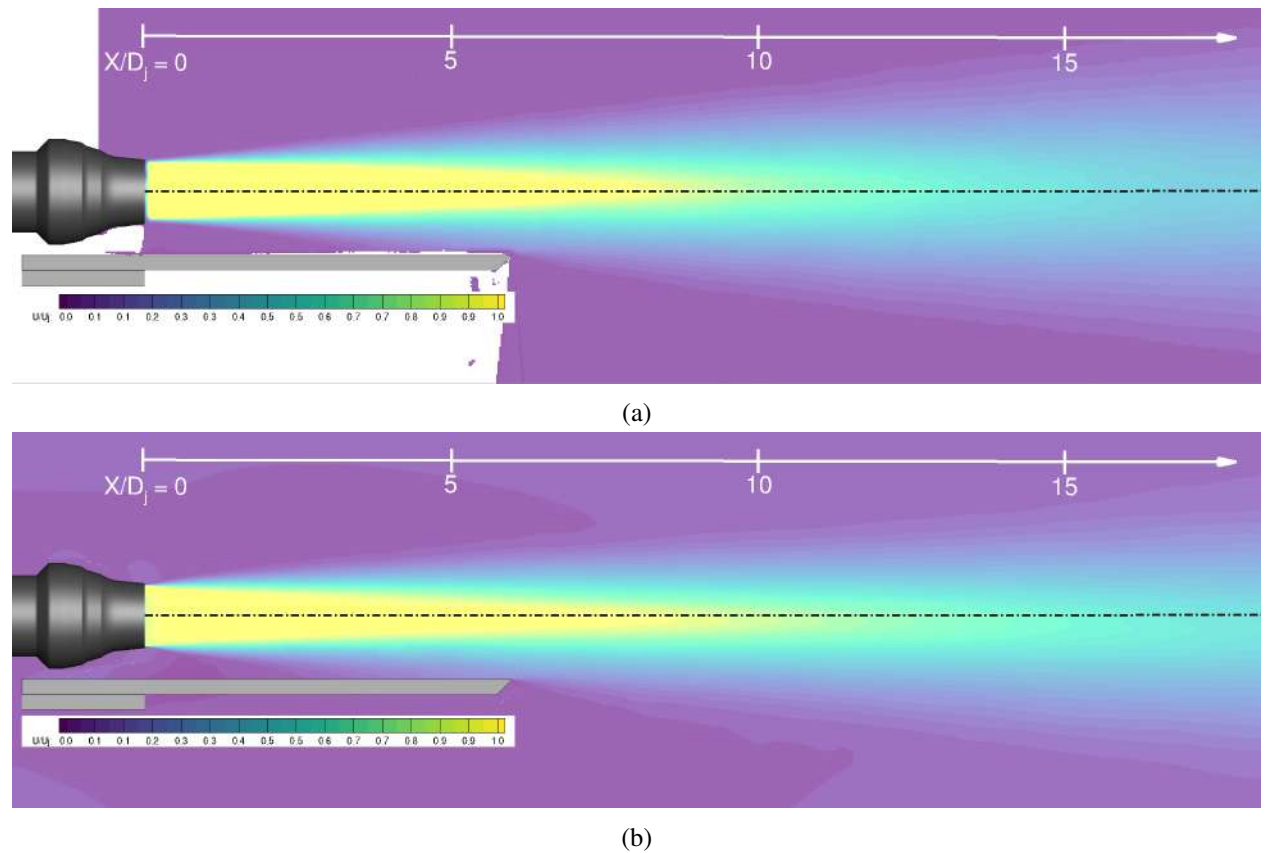


Fig. 17 Averaged axial velocity from (a) Experiments PIV of Brown & Bridges [17] (b) ZDES Mode III CFD simulation (250M). Jet Axis represented with dashed line.

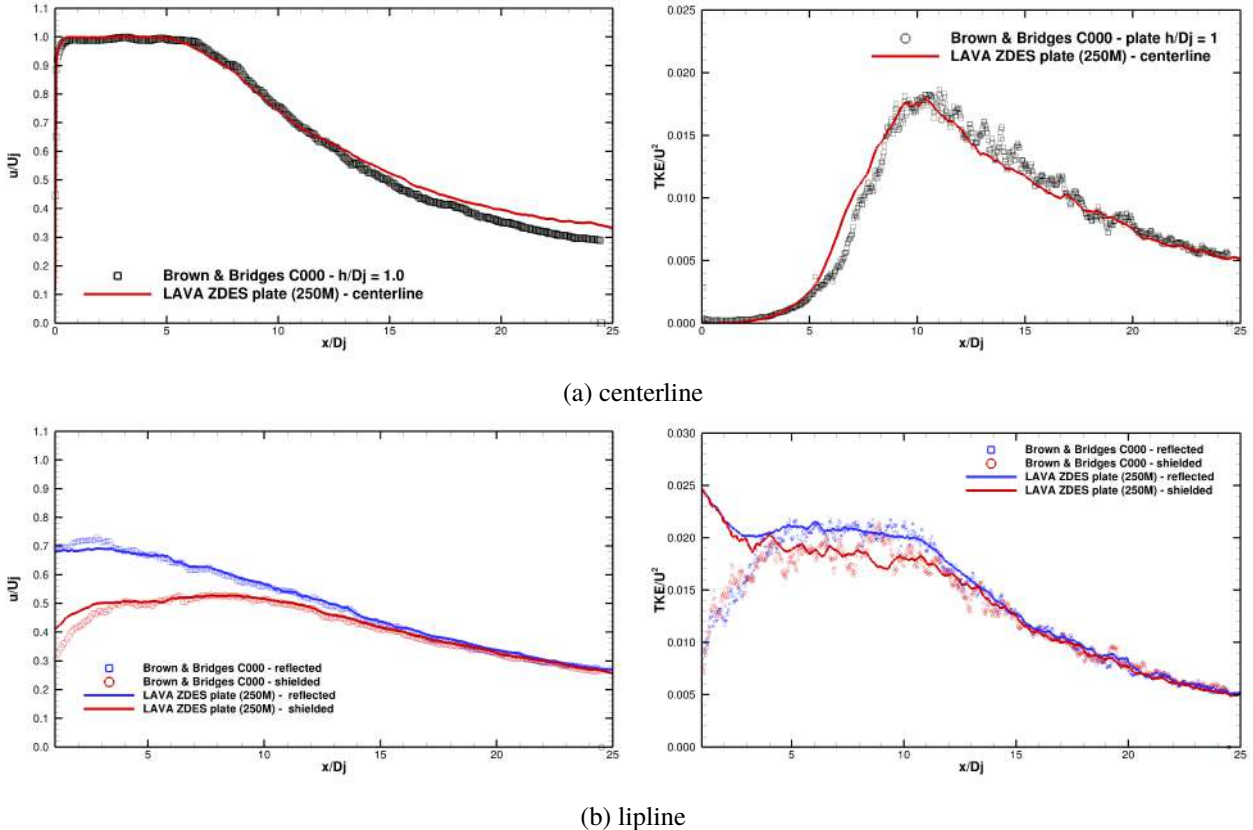
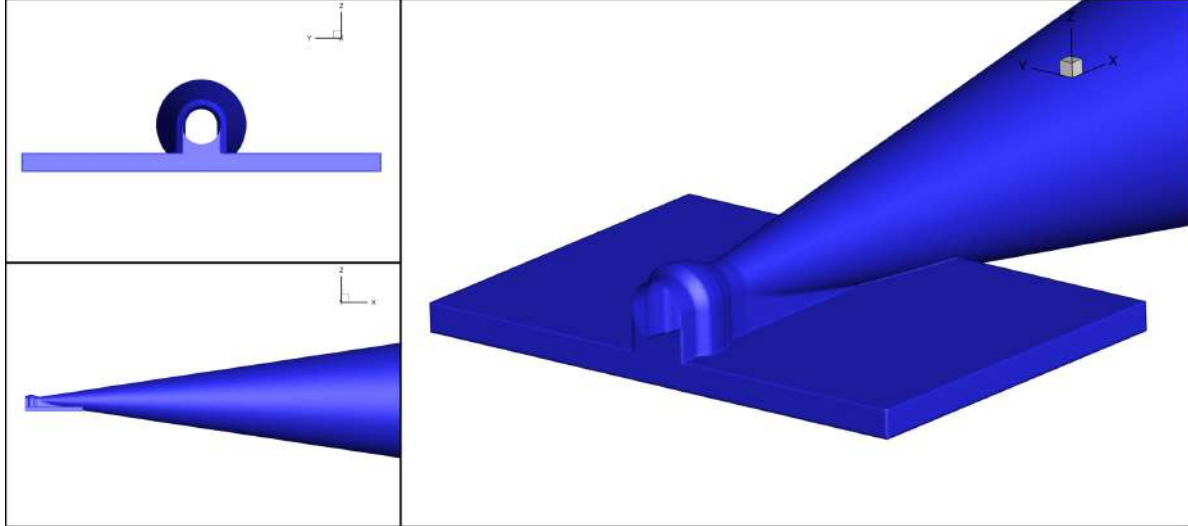
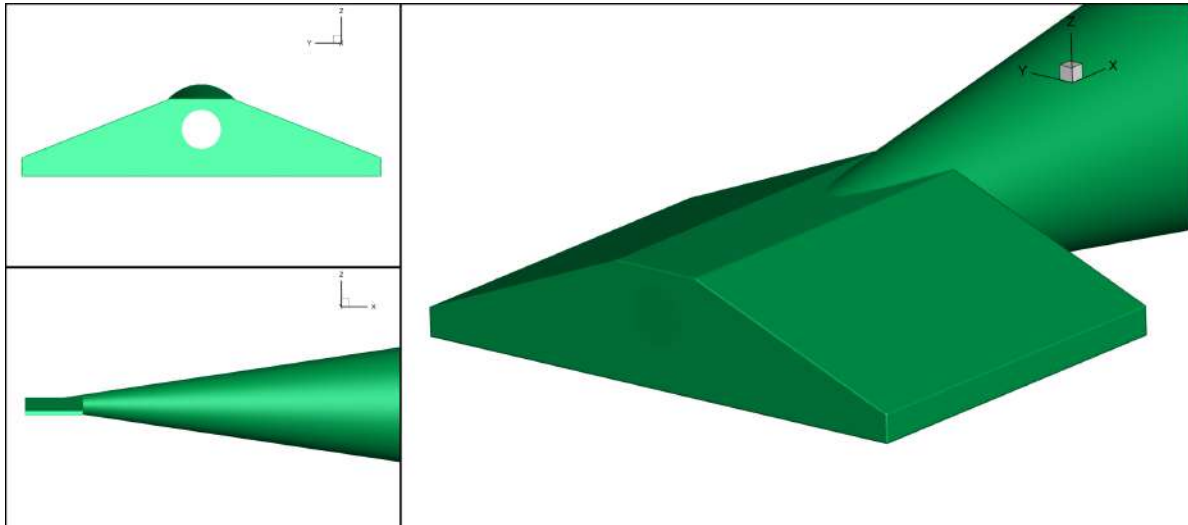


Fig. 18 Comparison of turbulent axial velocity statistics and turbulent kinetic energy between the LAVA ZDES Mode III simulation on the plate mesh (250M) and experiments by Brown & Bridges [15] on the (a) center-line, (b) lip-line. Where measurements compared at the reflected side are taken at $y/D_j = 0.5$ and shielded side at $y/D_j = -0.5$.

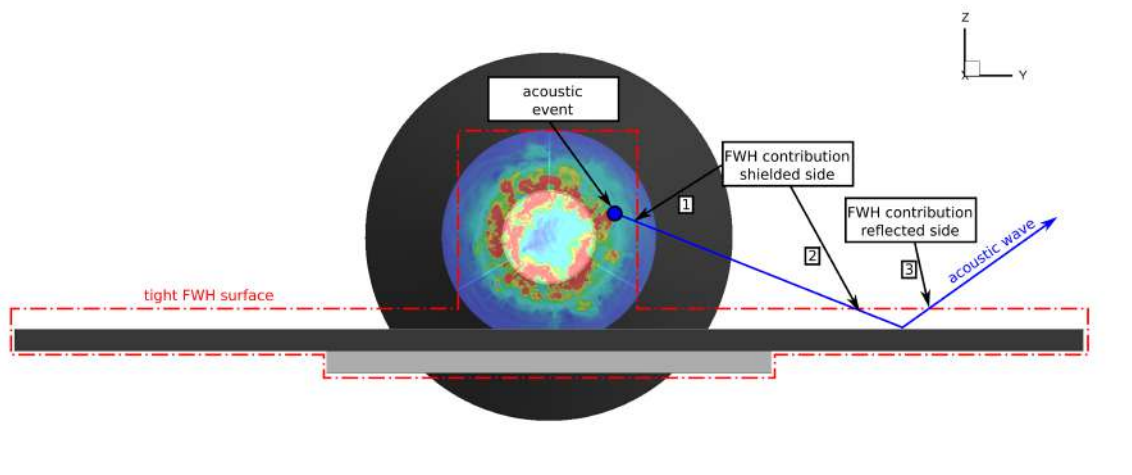


(a) Tight FWH surface

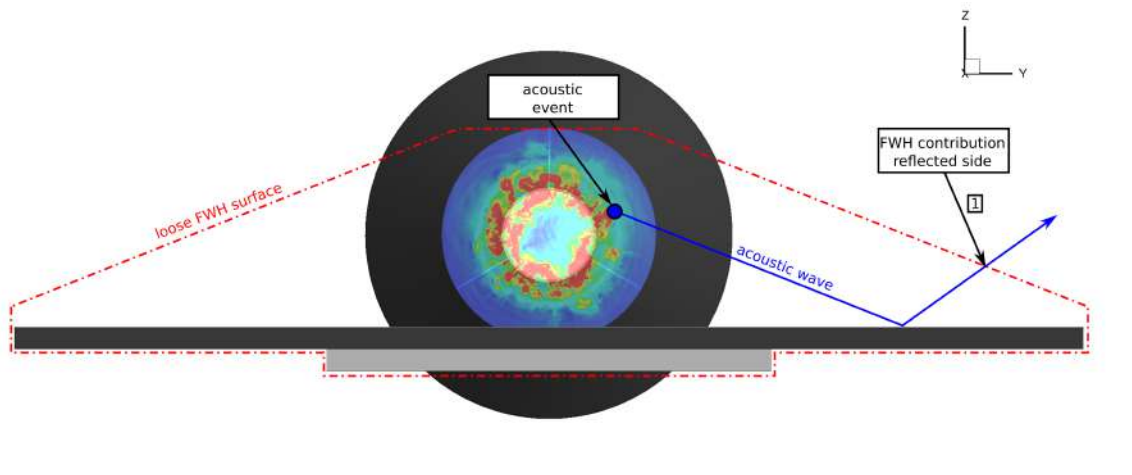


(b) Loose FWH surface

Fig. 19 Contour of the two different permeable Ffowcs Williams-Hawkins (FWH) surface triangulation's for the plate surface interaction simulation. Lower base of enclosing plate as well as cone extending from plate are consistent for both surfaces. Slope of conical section 0.10 with start of radial flare at $y/D_j = 0.60$ is intersected with loose and tight plate surface envelope. Surface triangulation has been automatically adapted to ensure proper resolution, which resulted in a mesh surface count of 600K triangles. End-cap averaging (25) has been utilized between $25D_j$ and $30D_j$.



(a) Tight FWH surface



(b) Loose FWH surface

Fig. 20 Sketch of contributions to (a) tight (b) loose FWH surface of an acoustic wave propagating towards and getting reflected by plate surface at high frequency. Contour plot of pressure gradient magnitude of isolated case added for visualization purposes, not representative of the actual case.

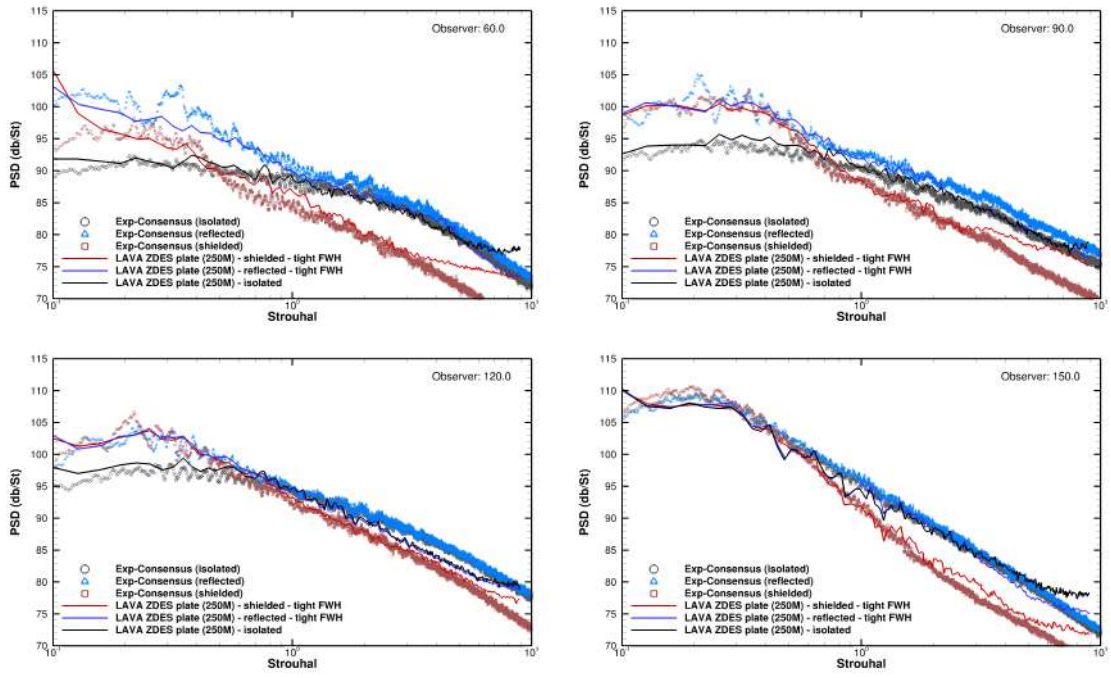


Fig. 21 Comparison of noise spectra between experimental consensus and ZDES Mode III at $100D_j$ using tight permeable FWH surface triangulation.

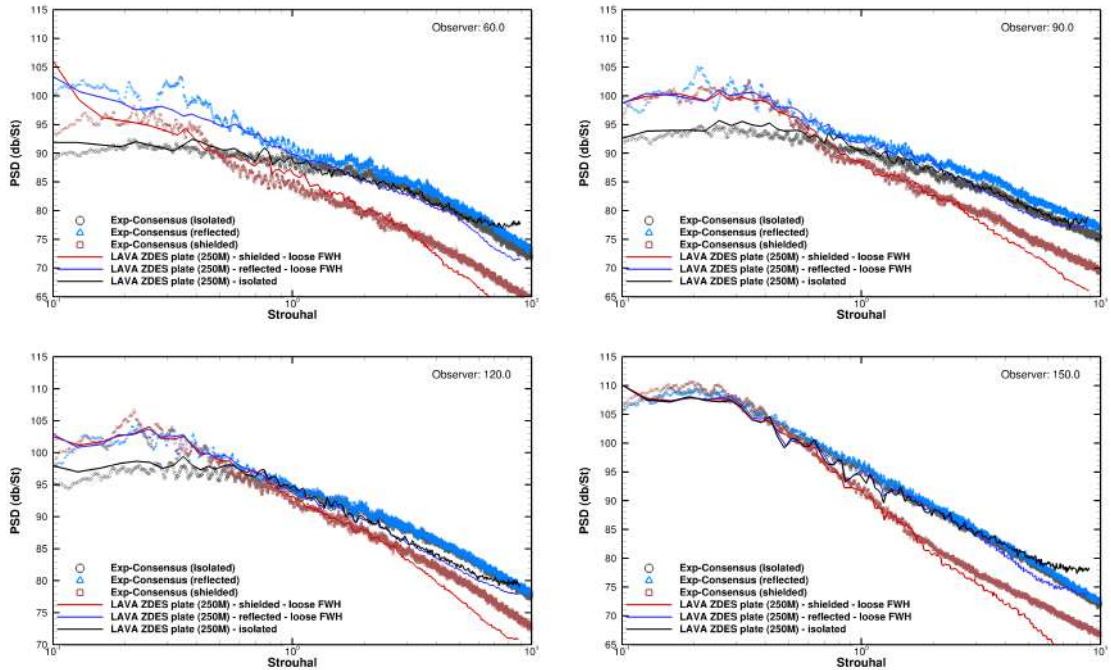


Fig. 22 Comparison of noise spectra between experimental consensus and ZDES Mode III at $100D_j$ using loose permeable FWH surface triangulation.